Technical Report:

Low-Cost Air Data Instruments for fixed-wing UAVs

Calibration and Discussion

George Zogopoulos - Papaliakos
PhD Student
gzogop@mail.ntua.gr

Paris Vaiopoulos
Diploma Student
pvaiopoulos@gmail.com

Supervisor:
Kostas J. Kyriakopoulos
kkyria@mail.ntua.gr

National Technical University of Athens
School of Mechanical Engineering
Control Systems Laboratory

Athens , April 5, 2017

Special thanks to Prof. D. Mathioulakis and Dr. M. Manolesos for their hospitality in the wind tunnel and their assistance during the calibration tests.

Document version: 1.2

Contents

List of Figures

List of Tables

Revision History

Revision	Date	Author(s)	Description
0.1	2016-11-16	GZP	Beginning of authoring
0.2	2016-12-02	GZP, PV	Finished document structure
0.8	2016-12-12	GZP	Pre-release version completed
1.0	2016-12-17	GZP	Release version
1.1	2017-03-24	PV	Revisited Pitot calibration model
1.2	2017-04-05	GZP	Added executive summary chapter

Chapter 1

Abstract

Airspeed (V_a), Angle-of-Attack (AoA, α) and Angle-of-Sideslip (AoS, β) sensors are indispensable measurement equipment for any aircraft parameter identification scheme. However, regarding small fixed-wing Unmanned Aerial Vehicles (UAVs), such sensors are considered an exotic and expensive piece of equipment. Since air data information was required for our research, we have integrated in our experimental fixed-wing UAV a low-cost (sub $200) air data system. To alleviate the uncertainty problems, stemming for this custom solution, a tailor-made calibration rig was constructed and calibration experiments were carried out in a wind-tunnel. Results reveal that our solution satisfies our needs and is competitive to similar solutions, employed by other research groups.

Chapter 2

Executive Summary

2.1 Introduction

The measurement of airdata quantities is indispensable for the development of any high-end, fixed-wing UAV, just as it is mandatory in manned aviation. Specifically, we are referring to the measurement of airspeed (V_a), angle-of-attack (AoA, α) and angle-of-sideslip (AoS, β). These quantities are indispensable for aerodynamic identification procedures, control systems designs and fault diagnostic systems.

The details of the measurement procedure are well understood in manned aviation and are incorporated into suitable sensor suites. As a result, reliable, redundant yet large, heavy, expensive and power-hungry instruments have been developed.

However, these instruments are not suitable for use in small-scale UAVs; downsizing in all aspects is required before they can be integrated in low-cost, low-weight airframes. Instead, in low-end research and commercial endeavors, ad-hoc solutions are used, with little evidence on their accuracy and suitability.

A prominent example is an ubiquitous small Pitot-static probe design, which is embedded in most low-end fixed-wing UAVs, despite theoretical indications that it is misused. In most cases, its small length does not allow its tip to reach in front of the increased pressure distribution created by the airframe. Wind vanes for AoA and AoS measurement are similarly affected.

In this work, we calibrated our available sensor suite for airspeed, AoA and AoS measurement in a wind tunnel in an effort to assess their suitability for our small-scale fixed-wing UAVs.

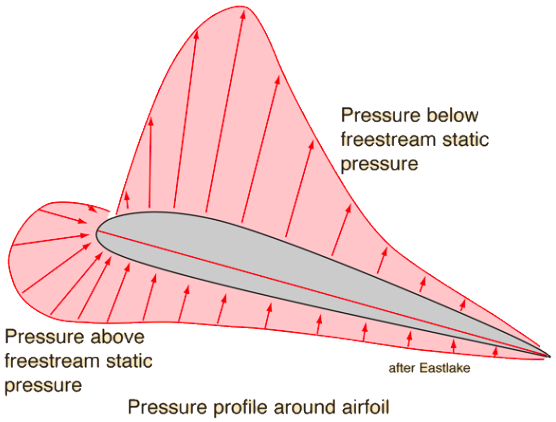

Typical pressure distribution around a moving airfoil

2.2 Sensor Suite

In this calibration, we used and compared the following instruments:

For airspeed measurement

- Hobby-grade Pitot-static probe
- 8mm Pitot-static probe by BasicAirData
- MPXV7002DP differential pressure sensor
- MS4525DO-DS5AI001D differential pressure sensor

A dominant hobby-grade Pitot-static probe design

For wind angle measurements we used a low-cost, Commercial-Off-The-Shelf angular encode with a custom 3D printed fin.

The combined sensor table can be seen below

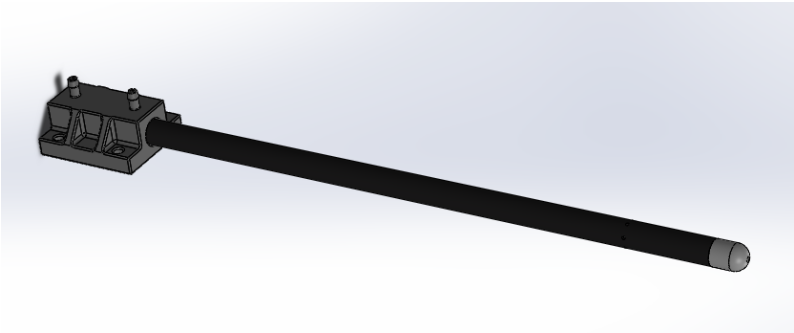

The BasicAirData 8mmESP probe

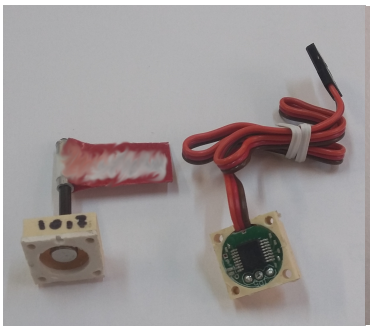

The COTS angular encoder

Vane fin

Sensor codename	**Mechanical Interface**	**Electrical Interface**
airspeed sensor 1	BasicAirData 8mmESP	MPXV7002DP
airspeed sensor 2	Hobby Pitot-Static probe	MPXV7002DP
airspeed sensor 3	Hobby Pitot-Static probe	MS4525DO-DS5AI001D
AoA sensor 1	Custom wind vane	Analog COTS sensor based on AS5040
AoA sensor 2	Custom wind vane	Analog COTS sensor based on AS5040
AoA sensor 3	Custom wind vane	Analog COTS sensor based on AS5040

The instruments were mounted on a motorized mount, governed by a microcontroller and placed into a wind tunnel. A range of test runs were carried out, sweeping a wide range of airspeeds and wind angles. A removable airfoil was used to emulate the effect of a wing onto the differential pressure measurements.

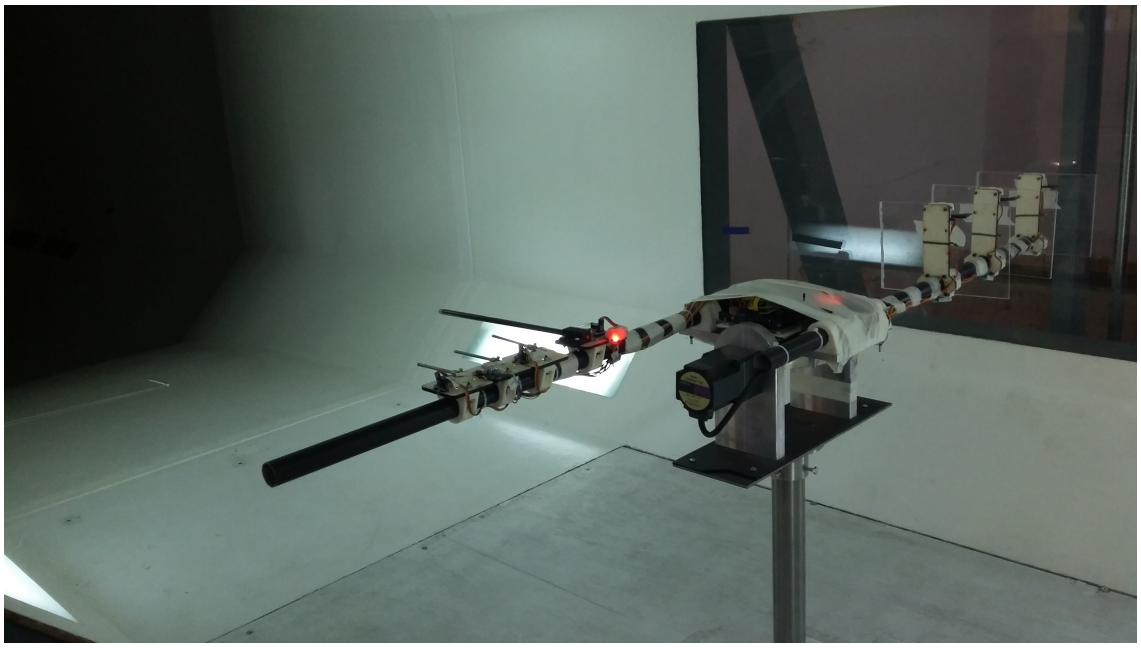

The automatic calibrator

2.3 Angle-of-Attack Measurement

For this array of tests, we consider the problems of measuring AoA and AoS identical and approach them with the same methodology. We mounted the wind vanes on standoffs, away from any obstacles, to measure their performance.

A typical uncompensated response can be seen below. A significant offset is evident as well as a less pronounced scaling error.

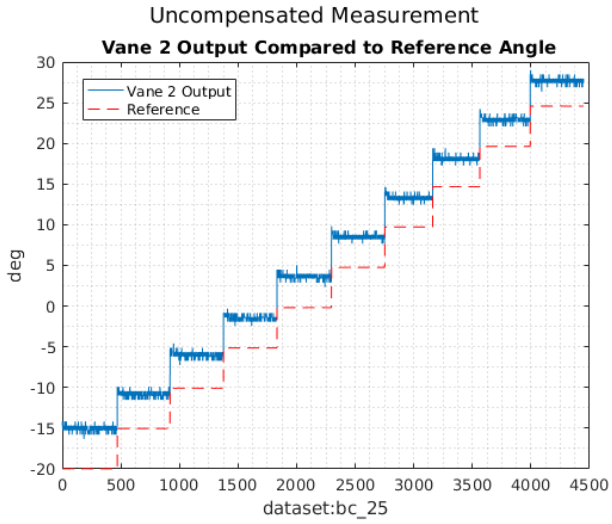

Comparison Between Vane & Reference Outputs

We proceeded with employing the calibration model of

$$\alpha_i = \theta_0 + \theta_\alpha \alpha_r$$

to fit the measurements and the corresponding errors, using an Ordinary Least Squares method. Afterwards, we carried out validation runs where we compared the compensated measurements with the reference.

The following tables summarize the results.

AoA sensor 1 calibration coefficients		
Parameter name	**Parameter value**	**Error bounds (95% - white)**
θ_0	3.9017	$\pm$0.0054
θ_α	1.1370	$\pm$0.0007
R^2	0.9923	
AoA sensor 2 calibration coefficients		
Parameter name	**Parameter value**	**Error bounds (95% - white)**
θ_0	4.2905	$\pm$0.0056
θ_α	0.9518	$\pm$0.0018
R^2	0.9898	
AoA sensor 3 calibration coefficients		
Parameter name	**Parameter value**	**Error bounds (95% - white)**
θ_0	0.6730	$\pm$0.0052
θ_α	0.9760	$\pm$0.006
R^2	0.9902	

AoA sensors model validation			
Error metric	Sensor 1	Sensor 2	Sensor 3
MAE (deg)	0.54437	0.65930	0.7477
RMSE (deg)	0.68751	0.90803	0.89947

The results are especially encouraging and indicate that any reasonably low-friction angular encoder can be used to capture perfectly usable AoA and AoS data, as long as they are presented with an undisturbed free airstream.

2.4 Airspeed Measurement

We proceed to airspeed measurement, which primarily comes down to measuring the differential between the ambient, static pressure and the dynamic, total pressure.

A first source of measurement error is the offset of the differential pressure sensor, a well-known occurrence. This is usually compensated for by recording the zero-input measurement of the sensor and for that reason we do not deal with this problem in our analysis.

We recorded the response of all 3 airspeed sensors, while induced to a range of incidence angles $\alpha \in [-20, 25]\,^\circ$, without a wing installed. The sensor responses can be seen below.

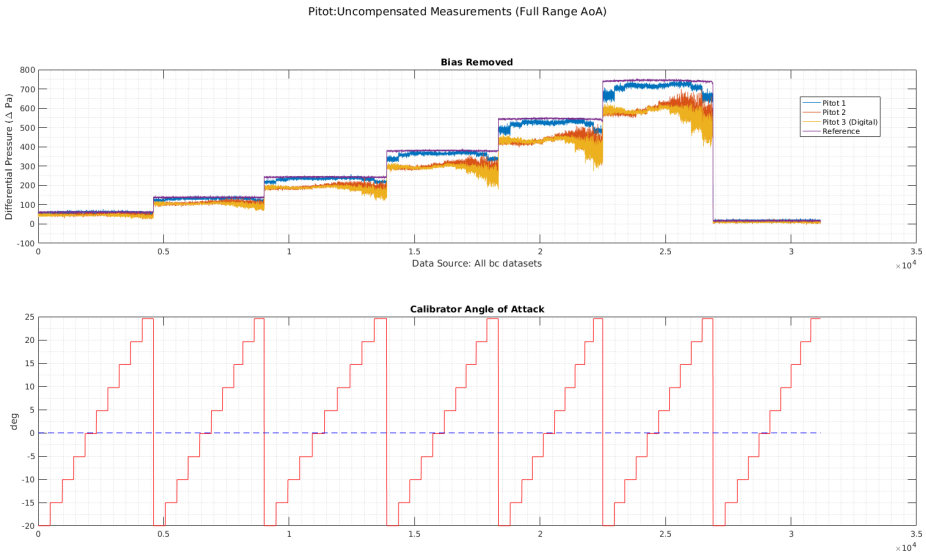

Uncompensated measurements - full AoA range

Sensor 1 is equipped with the BasicAirData probe, while the other two are using the hobby-grade probe. It is evident that sensors 2 and 3 have significant scaling errors, but on top of that, they are strongly dependent on the angle of attack. The effect of AoA on sensor 1 is much less pronounced. The following table contains the error statistics:

instrument	sensor 1	sensor 2	sensor 3
MAE (Pa)	16.22	63.78	71.71
RMSE (Pa)	23.74	82.82	92.06

Initially, we opted to construct a calibration model for use only within the range $\alpha \in [-5, 15]\,^\circ$, with $P_{d,r}$ as a regressor. The calibration coefficients and the validation errors turned out to be

instrument	$\theta_{P_{d,r}}$	R^2
sensor 1	0.9670 ±0.0001	0.9991
sensor 2	0.8100 ±0.0002	0.9967
sensor 3	0.7826 ±0.0002	0.9973

Instrument	sensor 1	sensor 2	sensor 3
MAE (Pa)	3.8047	6.7009	6.4057
RMSE (Pa)	4.9923	9.8628	8.9747

However, this model was not adequately accurate for the full AoA range, where the influence of the AoA was much more significant. Instead, we used the calibration model

$$z = P_{d,r}(\theta_0 + \theta_1|\alpha| + \theta_2\alpha^2)$$

with the following results:

instrument	θ_0	θ_1	θ_2	R^2
sensor 1	0.9523 $\pm 2.97 \cdot 10^{-4}$	0.049 $\pm 5.76 \cdot 10^{-5}$	-0.00031 $\pm 3.91 \cdot 10^{-6}$	0.9988
sensor 2	0.7963 $\pm 5.02 \cdot 10^{-4}$	0.003 $\pm 9.70 \cdot 10^{-5}$	-0.00021 $\pm 3.91 \cdot 10^{-6}$	0.9955
sensor 3	0.7809 $\pm 4.86 \cdot 10^{-4}$	0.038 $\pm 9.39 \cdot 10^{-5}$	-0.00030 $\pm 3.78 \cdot 10^{-6}$	0.9955

Instrument	sensor 1	sensor 2	sensor 3
MAE (Pa)	4.7006	8.4332	8.6530
RMSE (Pa)	6.7832	13.7502	14.1424

The presence of an airfoil on top of the calibrator rig made the calibration profile of the airspeed sensors no longer valid. Unfortunately, it was not possible to produce a new calibration model with adequate accuracy. However, the longer sensor 1 proved to be much less affected from the wing presence than the other two.

Another interesting topic is the comparison between the analog and digital differential pressure sensors. Even though the digital MS4525DO has better percent accuracy, it also has a wider measurement range, bringing it much closer to MPXV7002DP than expected. The comparison between sensor 2 and sensor 3 reveals this relation:

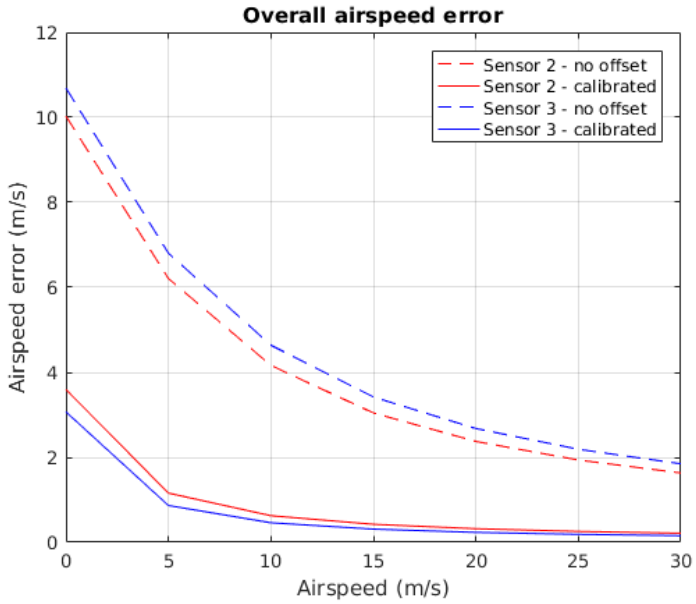

Airspeed error due to sensor error

2.5 Conclusion

Admittedly, the procedure of proper calibration for angle-of-attack vanes and Pitot-static probes is an involved and expensive one. However, our findings suggest that

- Any balanced wind vane on a low-friction angular encoder, placed in free stream can provide usable AoA and AoS readings
- In most applications, a 10cm-long Pitot probe is not adequate and introduces a lot of measurement error. The probe should be appropriately sized for the installation and the resulting measurements will be much more reliable.

Chapter 3

Introduction

3.1 On the lack of parameter information

One major research direction of our laboratory is that of fault detection in fixed-wing Unmanned Aerial Vehicles (UAVs). A broad range of faults are considered, including sensor, actuator, power-plant and aerodynamic faults. Model-based techniques are employed to construct residual signals which can serve as the basis of fault detection and isolation.

Specifically regarding faults in the aerodynamic structure and response of the aircraft, model-based techniques require a reference aerodynamic model. Most commonly, in both manned and unmanned aviation, the aerodynamic model of an airplane is expressed as a set of functions, applied on the aircraft state and evaluated to produce the aerodynamic forces and torques applied on the airframe. These functions are **linear in the parameters** but may be **non-linear in the arguments**. A typical formulation of these functions can be seen below, with the expression for the lift force, but will be discussed more extensively further on:

$$L = \frac{1}{2}\rho V_a^2 \left(C_{L_0} + C_{L_\alpha}\alpha + C_{L_q}\frac{q}{2V_a} + C_{L_{\delta_e}}\delta_e \right) \tag{3.1}$$

where L is the lift force, ρ is the air density, V_a is the airspeed norm, α is the Angle-of-Attack (AoA) and δ_e is the elevator deflection.

The aerodynamic model parameters encapsulate the flight characteristics of any airframe: its glide profile, its maneuverability, its stability etc. Alas, their values are almost never exactly known. Manned aviation aircraft manufacturers may provide parameter values for their models, but there certainly is no obligation to do so. Certified, high-precision aircraft simulator software written for large commercial airliners and fighter planes may be programmed by the aircraft designers, who have access to the airframe parameters. However, the numerical models found in lower-grade airplane simulation software may be the result of the combination of diverse sources of information, such as glide characteristics, sparse specifications and pilot "feeling".

The lack of information is even more severe in small unmanned aircraft, produced by smaller manufacturers. The design cycle for such aircraft is drastically shorter, which leaves little time for collected and documented aircraft parameter identification and validation experiments. If a design satisfies the required performance goals, no further examination is carried out regarding the aerodynamic parameters.

Institutes carrying out UAV-related research are those which suffer the greatest due to this lack of information. They often base their experimental platforms on converted model-aircraft, which come with absolutely no aerodynamic specifications. However, they require accurate aerodynamic parameter values on which to base control and estimation algorithms. As a result, it is not uncommon to set up parameter identification experiments prior to any further research effort. For this very reason, our laboratory carries out parameter identification experiments for each new flying platform.

3.2 The importance of air data

A reasonable assumption would be that the aerodynamic model of an aircraft would be a function of its state vector. As a reference, the established 12-DoF state vector for airplanes is comprised of:

- Inertial position
- Inertial velocity
- Attitude
- Angular velocity

However, this is not accurate, because the *aerodynamic model* is primarily affected by the air moving around the airplane. The relative motion of the airplane in reference to the air mass (in magnitude and direction) is the primary argument of the aerodynamic functions. This relative motion cannot be captured by the state vector of the aircraft, because it does not include the motion of the air mass in reference to the inertial frame. The most intuitive form of air mass motion is wind and is prevalent in all real-world experiments, despite the fact that it is often disregarded, for simplicity in theoretical derivations.

With the assumption that the air mass does not rotate in reference to the inertial frame, the effect of its relative motion in reference to the aircraft is encapsulated into three variables, often quoted as **air data**:

1. **airspeed**, V_a
2. **Angle of Attack**, AoA, α

3. **Angle of Sideslip**, AoS, β

The definition of these three quantities follows. Let the inertial velocity vector of the airplane be

$$\boldsymbol{v}_i = [u \; v \; w]^\mathsf{T} \tag{3.2}$$

and the velocity vector of the airmass be

$$\boldsymbol{v}_w = [u_w \; v_w \; w_w]^\mathsf{T} \tag{3.3}$$

The relative velocity vector is defined as

$$\boldsymbol{v}_r = \boldsymbol{v}_i - \boldsymbol{v}_w = [u_r \; v_r \; w_r]^\mathsf{T} \tag{3.4}$$

Equation 3.4 is often termed as the *wind triangle*, depicted in Figure 3.1.

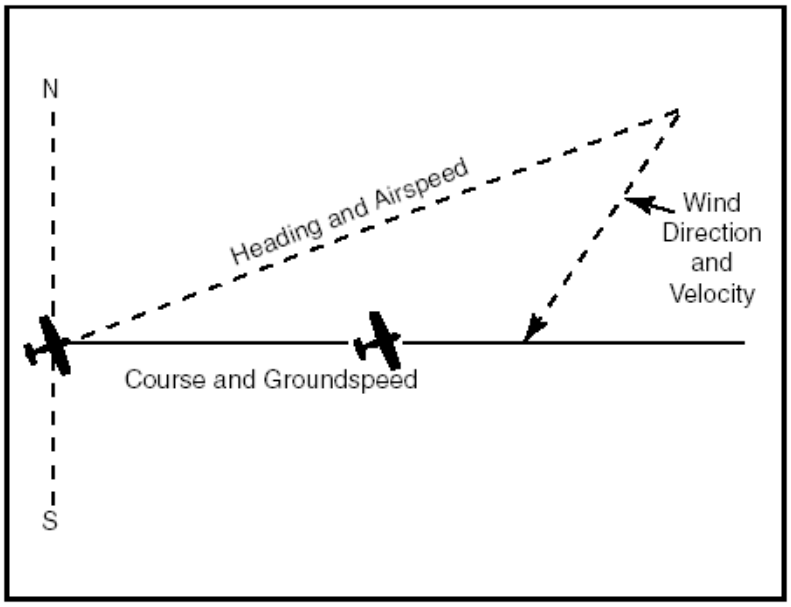

Figure 3.1: The wind triangle

With these definitions available, we can now proceed to define the air data components as

$$V_a = \|\boldsymbol{v}_r\| \tag{3.5}$$

$$\alpha = tan^{-1}(w_r/u_r) \tag{3.6}$$

$$\beta = sin^{-1}(v_r/V_a) \tag{3.7}$$

Air data components always appear in the formulation of the aerodynamic model, which most commonly is a variant of the form

$$F_D = \bar{q}S\left(C_{D_0} + C_{D_\alpha}\alpha + C_{D_\beta}\beta + C_{D_q}\frac{c}{2V_a}q\right) \tag{3.8a}$$

$$F_L = \bar{q}S\left(C_{L_0} + C_{L_\alpha}\alpha + C_{L_q}\frac{c}{2V_a}q\right) \tag{3.8b}$$

$$F_Y = \bar{q}S\left(C_{Y_\beta}\beta + C_{Y_r}\frac{b}{2V_a}r\right) \tag{3.8c}$$

$$l = \bar{q}Sb\left(C_{l_0} + C_{l_\beta}\beta + C_{l_q}\frac{b}{2V_a}q + C_{l_{\delta_a}}\delta_a\right) \tag{3.8d}$$

$$m = \bar{q}Sc\left(C_{m_0} + C_{m_\alpha}\alpha + C_{m_q}\frac{c}{2V_a}q + C_{m_{\delta_e}}\delta_e\right) \tag{3.8e}$$

$$n = \bar{q}Sb\left(C_{n_0} + C_{n_\beta}\beta + C_{n_r}\frac{b}{2V_a}r + C_{n_{\delta_r}}\delta_r\right) \tag{3.8f}$$

Each of the above equations is a model of the drag, lift, sideforce, roll moment, pitch moment and yaw moment respectively.

The model coefficients which correspond to the AoA and AoS characterize the tendency of the aircraft to align itself with the relative wind vector. The coefficients corresponding to the angular rates describe the damping characteristics of the airframe. Finally, the coefficients which correspond to the control inputs express the sensitivity of the aircraft to those inputs.

Thus, it becomes apparent that the aerodynamic model of any airplane is a function primarily on angular rates, control inputs and the air data.

3.3 Measuring air data

Common airframe setups

Parameter identification algorithms and techniques usually record the aerodynamic model arguments and response (output) and try to find parameter values which are a best-fit for the previous equation set. The control inputs are user-defined and considered known. The aerodynamic forces are measured with accelerometers and torques are measured with gyroscopes. Modern MEMS sensors are both lightweight and accurate enough to serve this purpose. This leaves air-data as the only remaining information required for parameter identification.

Classically, airspeed is measured with a Pitot-static probe (Figure 3.2), attached to a differential pressure sensor. Through the Bernoulli equation, the recorded differential pressure can be converted to indicated airspeed [7].

AoA and AoS measurement at its most basic form can be carried out with simple wind-vanes, whose angle is measured by an appropriate sensor, such as an angular encoder (Figure 3.3).

Figure 3.2: A common Pitot-static probe design

Figure 3.3: An angle-of-attack sensor installed on a passenger airplane

However, different sensor suites are used for air data measurement, as a response to mechanical and fluid dynamics challenges, which may rise on specific installation scenarios.

Large transport aircraft, whose autopilot software requires accurate reading of the air data from multiple, redundant sensors, may employ a collection of probes, vanes and multi-hole probes (Figure 3.4).

Fighter aircraft, also need accurate airspeed and and AoA measurements but in a more compact and ruggedized form-factor. Air data booms may be found in experimental setups as well (Figure 3.5).

Personal airplanes also carry airspeed sensors (Figure 3.6). AoA sensors may not be found on this type of airplane, since the pilot, who has direct control over the aircraft, has a sense of the AoA and can regulate the flight trim state based on this "internal reference".

AoA sensors can still be found on personal aviation aircraft, in the form of multihole probes while new experimental sensor designs are introduced [12] (Figure 3.7).

Figure 3.4: Multiple and redundant air data instruments on a passenger jet

Airspeed sensors are almost always found in commercial UAVs (Figure 3.8), since airspeed regulation is critical toward maximization of the effective range of the aircraft. AoA and AoS sensors are more rarely found on UAVs.

Figure 3.5: An airdata boom mounted on the nose of an experimental aircraft

Figure 3.6: A Pitot probe on a personal aircraft

Figure 3.7: The two-port sensor from [12]

Figure 3.8: A UAV equipped with a Pitot-static probe

Measurement difficulties

Air data measurement is considered a challenging task on any aircraft. The intended measurement is that of the magnitude and direction of the unperturbed relative air flow (free-stream measurement). However, the effect of the aircraft on its surrounding air is considerable and corrupts the measured quantities (Figure 3.9) (Image taken from http://hyperphysics.phy-astr.gsu.edu/hbase/Fluids/airfoil.html). At airspeeds where the air is considered an incompressible fluid, the wake of the aircraft body extends sideways and in front of it.

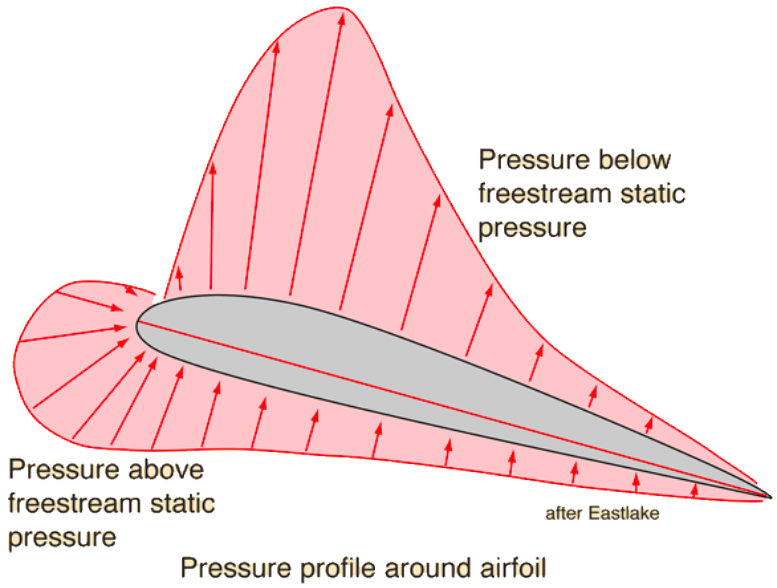

Figure 3.9: Typical pressure distribution around a moving airfoil

The air pressure around the aircraft body varies, affected by the aircraft geometry. As a result, the pressure recorded by the ports of the Pitot-static probe will differ from the actual static air pressure, resulting to measurement errors. Multi-hole AoA probes also suffer from the same problem.

The re-direction of the airflow over the aircraft geometry also affects the wind vane type sensors, which will report erroneous values.

On manned aviation aircraft, these problems are often addressed through calibration of the sensing systems, on carefully controlled environments (wind tunnels). This process is very data-intensive, difficult in its application and very expensive. While these costs are justified on manned aviation, unmanned systems rarely employ such procedures. On the contrary, in these cases efforts are made to place the sensing system as far in front of the airframe as possible, so that it resides in unperturbed airflow.

In practice, this approach also has its own problems, with the weight and rigidity of the sensor supporting beam being the limiting factors.

Due to all those limitations, the cost of air data measurement systems is often high, especially in the context of a small, low-cost UAV, becoming an unreasonably high-cost component of the UAV sensor suite.

In face of all the aforementioned problems, we have chosen to set up our own low-cost air data measurement system and evaluate its performance with a calibration session. Our reasoning was to assess the performance of the uncalibrated sensors and decide whether they can be fitted onto the aircraft without calibration. If this is not possible, then we would resort to traditional calibration techniques.

Chapter 4

Problem Formulation

Formally, the questions this work is called to answer are:

Given a

- Pitot-static probe, coupled to a differential pressure sensor and
- two wind vanes, coupled to an angular encoder each,

which will be used as an air data system in a fixed-wing small-scale Unmanned Aerial Vehicle, quantifiable results should be provided regarding:

1. The error statistics of the measurement system
2. The effect of the sensors installation position on the measured quantities
3. The extraction of a calibration (and possibly compensation) model for the overall air data system.

Statistical processing on wind tunnel tests shall be carried out to obtain experimental data on the questions at hand.

If these results do not meet the standards required for aircraft parameter identification, then the air data measurements should be fed into a (Extended) Kalman Filter for further processing and filtering.

Chapter 5

Sensor Suite

In this chapter, the instrumentation which was examined during this work will be presented. It consists of

- Pitot-static probes
- differential pressure sensors
- absolute pressure sensors
- wind vanes
- angular encoders

5.1 Pitot-static probes

Hobby Pitot-static probe

Figure 5.1: A dominant hobby-grade Pitot-static probe design

This design, sold by various manufacturers, is dominant in hobby-grade UAVs and can also be found in small research projects. It is being sold as the recommended probe in all ArduPilot autopilot kits, as well as in the Paparazzi and EagleTree systems [5, 3].

It consists of two short 80mm concentric metal tubes, capped with a metal head of non-specific geometry. The external diameter is 4.1 mm.

While this design is being used in a great number of UAVs, there are very few reports on its performance, mostly because the expectations and specifications of these aircraft are very low. Some theoretical and experimental findings regarding this probe indicate that its length is likely to be insufficient for proper airspeed measurement [11, 8, 9].

Any results on this probe will be valuable, since a lot of systems rely on its performance for airspeed measurement.

BasicAirData 8mm probe

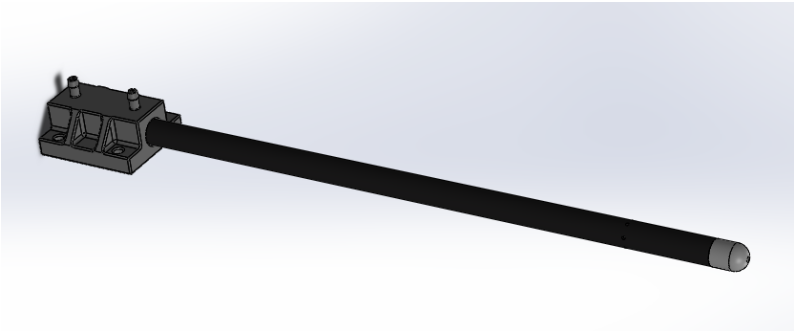

Figure 5.2: The BasicAirData 8mmESP probe

BasicAirData is an open-hardware and open-source collaborative project focused on the design of air data instruments. Its members have created multiple probe designs and articles on calibration and compensation. One of these designs is the *8mm Flanged Pitot*, reference name *8mmESP*.

The 8mm Pitot-static probe cannot be purchased but its designs are freely available online. Ours was a kind donation from one project member. The probe consists of two concentric carbon fiber tubes, a hemispherical, 3D printed probe head and a 3D printed mounting flange.

Numerical investigations on the rigidity of the probe have been carried out by its designers [10].

Our probe was 250 mm long, from the tip of the probe head to the beginning of the mounting flange.

5.2 Wind vane

(a) CAD model

(b) Complete vane

Figure 5.3: The custom-made wind vane

A magnetic angular encoder solution was used as an aerodynamic angle measurement sensor. A carbon fiber shaft was mounted on a small open ball bearing and fixed on a cubic enclosure. A magnet was fixed at the end of the shaft, inside the enclosure, to be coupled to a magnetic angle encoder. On the other end of the shaft, a 3D printed wind vane was fixed.

The wind vane needed to be balanced, so that its center of gravity lied on the shaft and gravity effects on the measured angle would be eliminated. To that goal a metal threaded rod was incorporated as the head of the wind vane and a nut was inserted on it. The nut was screwed as far back so as to balance the vane and then fixed with thread lock glue.

Proper balance was achieved by human inspection, but it should be noted that the shaft had a tendency to back-trace a few degrees of rotation, after movement to one-direction. This is attributed to surface tension of the bearing lubrication oil.

5.3 Differential pressure sensors

MPXV7002DP

This is a differential pressure sensor with analog output by NXP (Figure 5.4). It is rated for +-2kPa, with maximum rated offset ±6.25% and accuracy ±2.5% of the full range. It was widely used in the past in hobby-grade systems but is now considered an old part and its popularity has faded. This device is ratiometric. More details on its specifications can be found on the comparative Table 5.1.

MS4525DO-DS5AI001D

This, more modern, digital differential pressure sensor, manufactured by Measurement Specialties, has become more prominent in low-grade airspeed measurement systems (Figure 5.5). It has a digital, I^2C communication interface and an internal

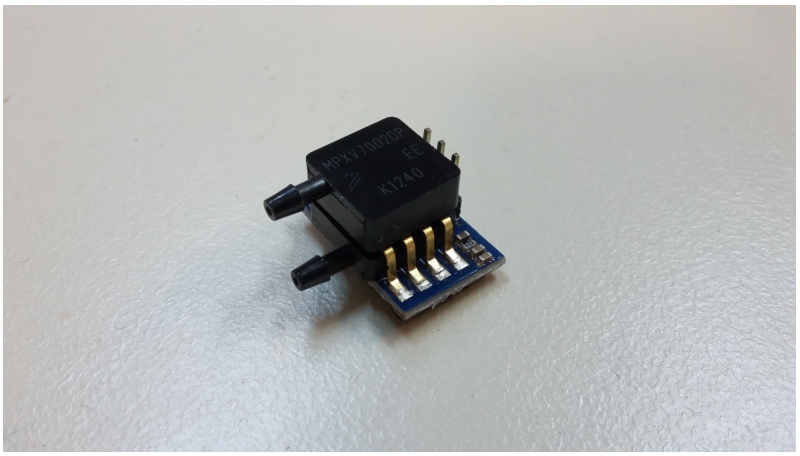

Figure 5.4: The MPXV7002 differential pressure sensor

Figure 5.5: The MPXV7002 differential pressure sensor

14-bit Analog-to-Digital Converter (ADC) which eliminates the need of an external ADC. It also has a greater measurement range compared to MPXV7002. Its specifications are summarized in Table 5.1.

In practice, as we shall see in later chapters, the actual error budgets are significantly lower, but a noticeable remark can be made: The greater resolution and relative accuracy of the MS4525DO are countered (in part) by its larger range, resulting in more modest absolute error.

instrument	MPXV7002DP	MS4525DO-DS5AI001D
Output Type	Analog	Digital (I^2C)
Supply Voltage	5V	5V
Measurement Range	±2 kPa	±1 psi (6.895 kPa)
Resolution **Maximum Offset**	N/A ±6.25% FSS	14-bit N/A
Typical Accuracy - Rel	±2.5% FSS	±0.25% FSS
Typical Accuracy - Abs	±100 Pa	±17 Pa

Table 5.1: Specifications table for the employed differential pressure sensors

5.4 Absolute pressure sensor

Bosch BMP085

Figure 5.6: The BMP085 absolute pressure sensor

An absolute pressure sensor (barometer) was employed to calculate the air density and convert differential pressure to airspeed measurements. The BMP085 is a digital I^2C device whose specifications can be seen in Table 5.2. The actual sensor used was part of an IMU breakout board, the *DFRobot 10-DOF IMU*.

Output Type	Digital (I^2C)
Supply Voltage	3.3V
Measurement Range	30 000 Pa to 110 000 Pa
Resolution	1 Pa
Typical Accuracy	±1 Pa

Table 5.2: Specifications of the Bosch BMP085 barometric sensor

5.5 Angular position encoder

COTS solution based on the AS5040

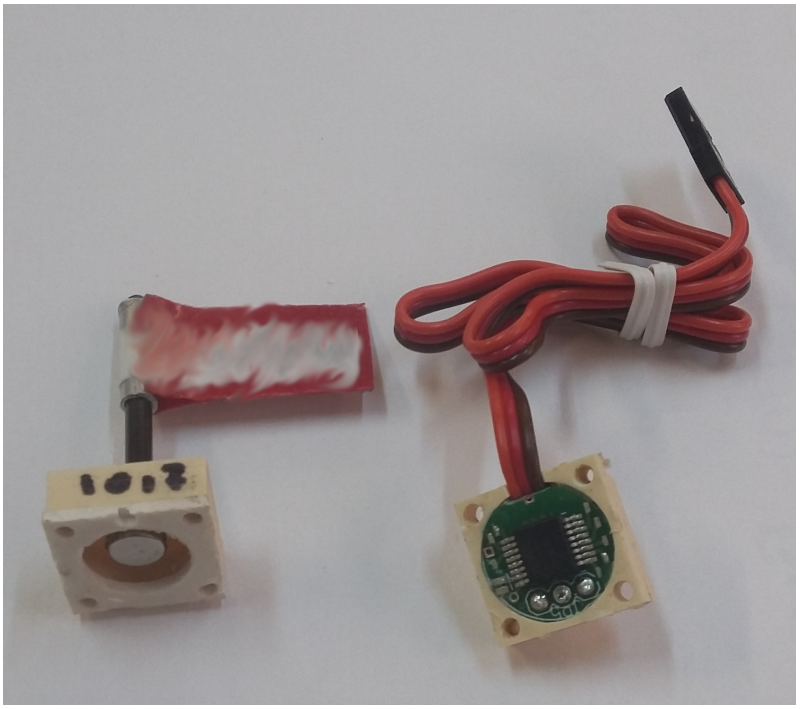

Figure 5.7: The COTS angular encoder

The AMS AS5040 360° magnetic rotary encoder is a programmable IC capable of 10-bit resolution. Although the IC itself has a digital and PWM output, the COTS product we used during our experiments implemented an RC low-pass filter to convert the PWM output into a continuous, analog output signal, ranging from 0V to 3.3V, for the full angular range. Even though its nominal resolution was 0.351°, in practice the output signal had significant noise superimposed, even though its mean value remained stable with stable angle input (Figure 5.8). No accuracy specifications were given.

In practice, the measurement fluctuation, when captured with a 10-bit Digital-to-Analog Converter (DAC) with significant averaging, was at the order of 3 Least Significant Digits (LSBs), which is equivalent to 1.6°.

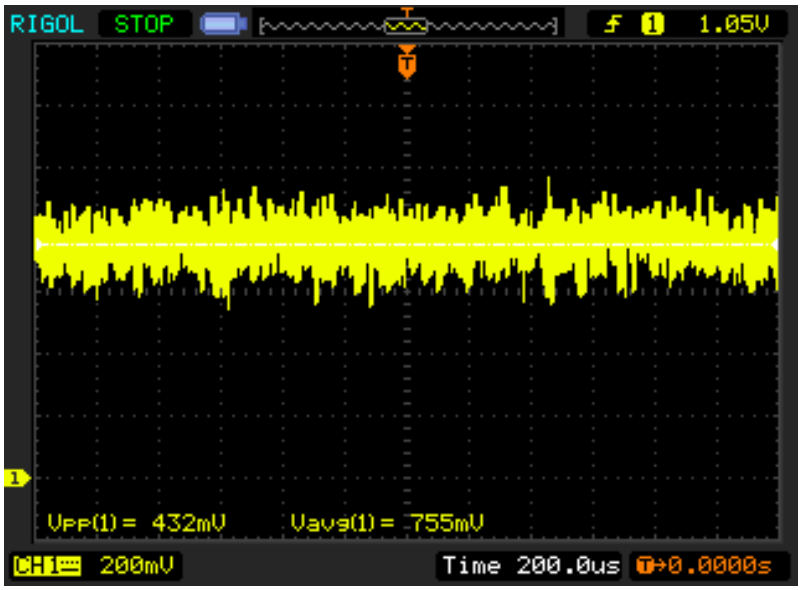

Figure 5.8: Noisy output from the angular encoder

5.6 Measurement System Configurations

With the intended test procedures in mind, the available probes and sensors were combined into specific configurations. Each configuration was given a codename and is presented in Table 5.3. These designations will be used throughout this report.

Sensor codename	**Mechanical Interface**	**Electrical Interface**
airspeed sensor 1	BasicAirData 8mmESP	MPXV7002DP
airspeed sensor 2	Hobby Pitot-Static probe	MPXV7002DP
airspeed sensor 3	Hobby Pitot-Static probe	MS4525DO-DS5AI001D
airspeed sensor 4	Hobby Pitot-Static probe	MPXV7002DP
AoA sensor 1	Custom wind vane	COTS sensor based on AS5040
AoA sensor 2	Custom wind vane	COTS sensor based on AS5040
AoA sensor 3	Custom wind vane	COTS sensor based on AS5040

Table 5.3: The sensor configurations which were tested

Chapter 6

Calibrator Setup

6.1 Supporting structure

A significant part of the experimental procedure would be to test the sensors under various angles of attack. Some of the sensors where AoA sensors after all! Thus, it would be necessary to have a precise and repeatable method to adjust the angle of the mounting structure where the sensors would reside.

One way to go about it would be to have an adjustable but fixed structure: its angle could be modified but then fixed (possibly with screws or clamps) during the test. This would be a significant burden for the experiment operator, because we were interested in testing for large resolutions of AoA (down to 0.5) degrees and performing a considerable amount of test runs. Stopping the wind tunnel, adjusting the probe mount and re-starting would quickly become tedious.

This is why we opted for a motorized sensor mount (Figure 6.2). A platform pitching about one axis, connected to an Oriental Motor ASM66AK-T20 stepper motor, with 4000 steps per revolution and rated torque of 3.5 N m. The structure was made of steel and was very rigid.

Due to the lack of space on top of the initial motorized platform, two aluminium plates were fastened on top of it, to create a platform of greater surface area.

The overall calibrator construction can be seen in Figure 6.1. Its overall dimensions were 140x32x29cm (WxLxH) and its weight was approximately 7 kg.

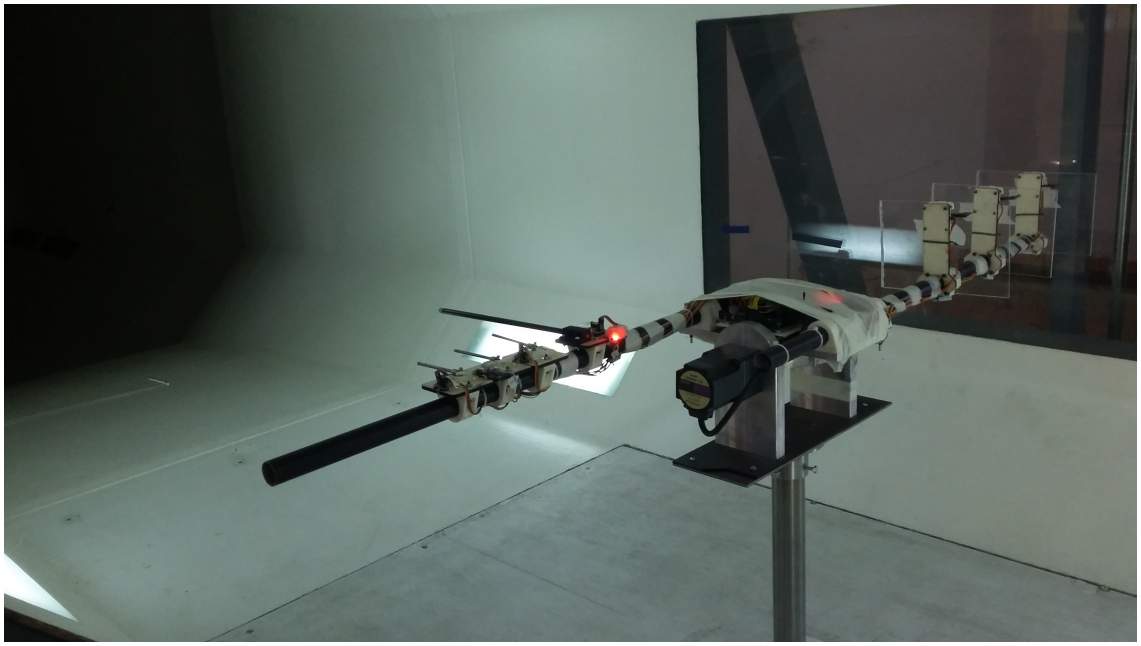

Figure 6.1: The automatic calibrator which was constructed for the experimental procedures

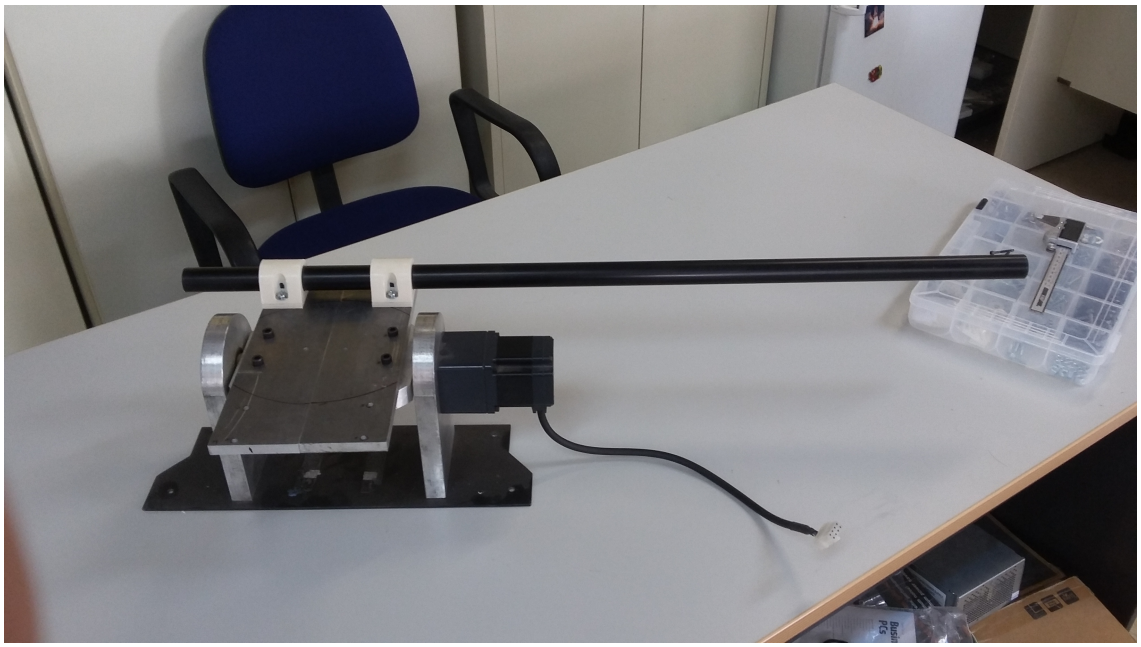

Figure 6.2: The pivoting base of the calibrator and one mounting tube

6.2 Sensor mounting

The sensors should be held far away and clear of the calibrator structure aerodynamic wake. To that goal, two aluminium hollow tubes were fixed on the pitching platform and extended outwards. The tubes were 85 cm long and their diameter was 25 mm. 3D printed ABS clamps were manufactured, which held the tubes firmly fixed (Figure 6.3).

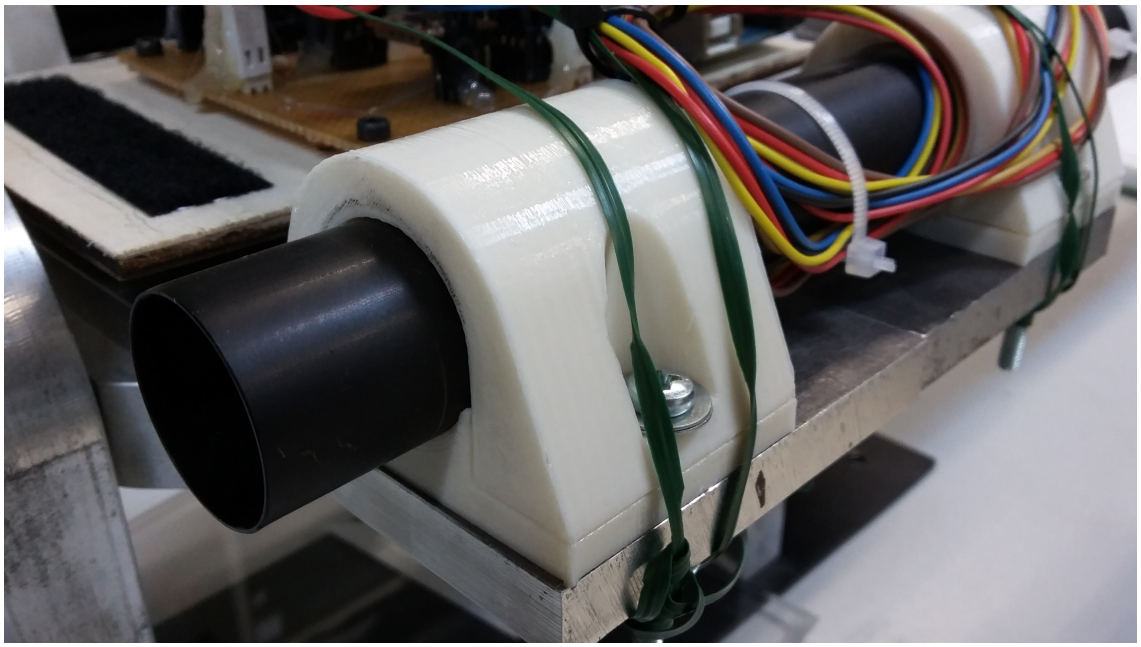

Figure 6.3: 3D printed mounts for the aluminium tubes

Pitot-static probes

Each airspeed sensor was mounted on the aluminum tube on a separate tray. A 3D printed ABS clamp would be fixed on the mount, hosting a plywood rectangular tray on top of it (Figure 6.4). The Pitot-static probes were screwed down to the wood and the differential pressure sensors were fixed either with screws or with Velcro and hot glue. The silicone pressure tubing was also rigidly fixed with hot glue, to prevent vibrations which would appear as measurement noise.

AoA vanes

The wind vanes do not have a naturally protruding geometry to extend to free stream, contrary to the Pitot probes. Thus a structure was constructed from plywood and 3D printed ABS to raise them above the mounting tube and onto cleaner air and provide a housing (Figure 6.5). Also, a plate of cast acrylic sheet was placed flush to the wind vane, to prevent turbulence from the supporting structure to affect its readings.

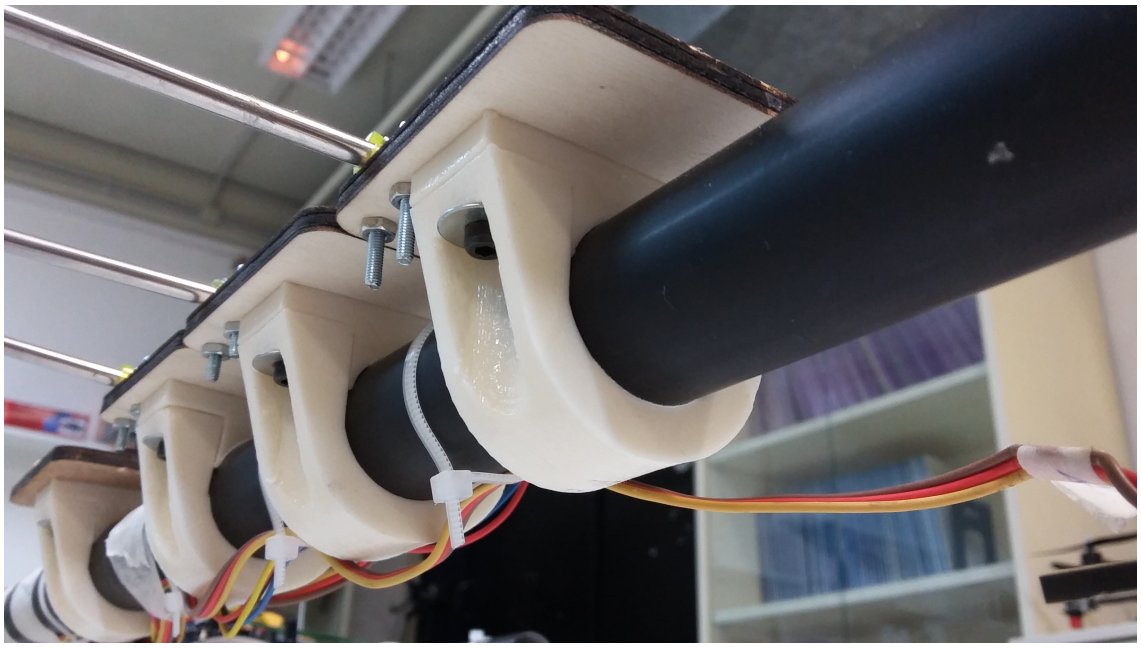

Figure 6.4: 3D printed mounts and wooden plates for the airspeed measurement systems

Barometer

The barometer was mounted alongside one of the Pitot-static probes and fastened with screws and nuts (Figure 6.6). The foam block placed over the sensing port serves as a dampening filter against pressure variations due to wind currents and light-induced heating.

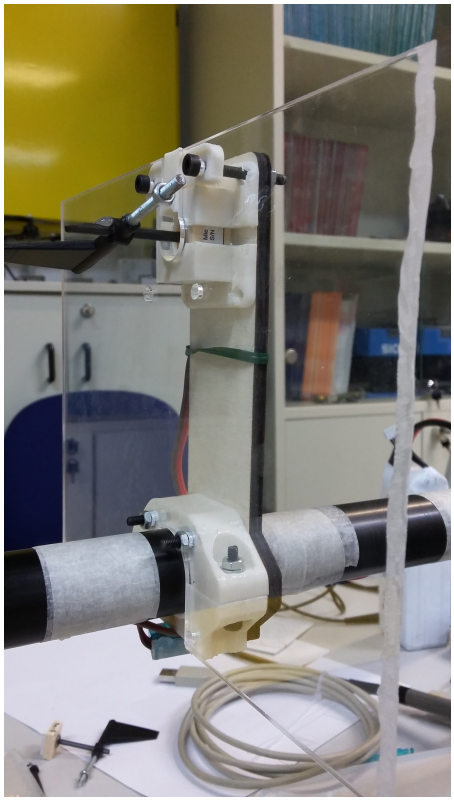

Figure 6.5: Wind vane mount, using a combination of 3D printed and laser-cut materials

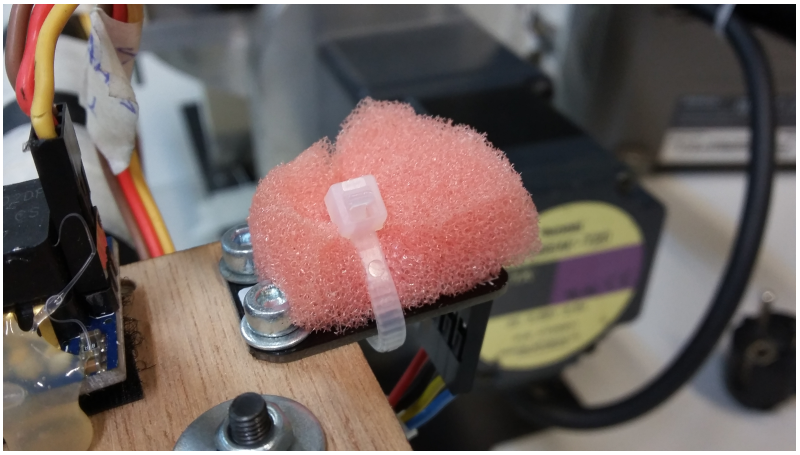

Figure 6.6: Barometer mounting detail

6.3 Wing mounting

In order to introduce the effect of a wing to the airspeed sensors, a foam wing, taken from an RC aircraft model was placed on top of the Pitot-static probes mounting plates (Figure 6.7). It was carved so that the probes and sensors would fit as far inside of it as possible and secured with wires on the aluminium tubes.

However, due to its relatively thin airfoil, it was impossible to enclose all of the calibrator geometry inside of the wing. As a result, parts of the probe mounts and the aluminium tube protruded under the wing, possibly differentiating the final geometry from a real-world sensor installation (Figure 6.8).

Figure 6.7: The calibrator with the wing installed

Figure 6.8: Protruding calibrator geometry under the wing

6.4 Control and data acquisition

An Arduino Mega 2560 microcontroller was dedicated to serve as the calibrator controller. It was programmed to interface with the sensors, control the pivoting platform and send the measurements wirelessly to a remote computer through a telemetry link.

The barometer and digital differential pressure sensor were mounted onto the I^2C bus of the microcontroller whereas the AoA sensors and analog differential pressure sensors were connected to analog inputs, sampled by 10-bit ADCs.

The control of the angle of the calibrator was achieved by interfacing the microcontroller with a stepper motor driver, placed adjacently. Rotation direction and speed were explicitly controlled, by two digital output signals.

Two datalogging programs were written and used separately. The first would only read the barometer pressure and temperature and send them serially over an XBee Pro 2.4 GHzradio to an identical receiver, connected to a computer. The second would sample the rest of the sensors and send a line containing all measurements over telemetry in a similar manner, while controlling the AoA profile.

The calibrator electronics were powered by a 3-cell LiPo battery.

An overall view of the electronics can be seen in Figure 6.9.

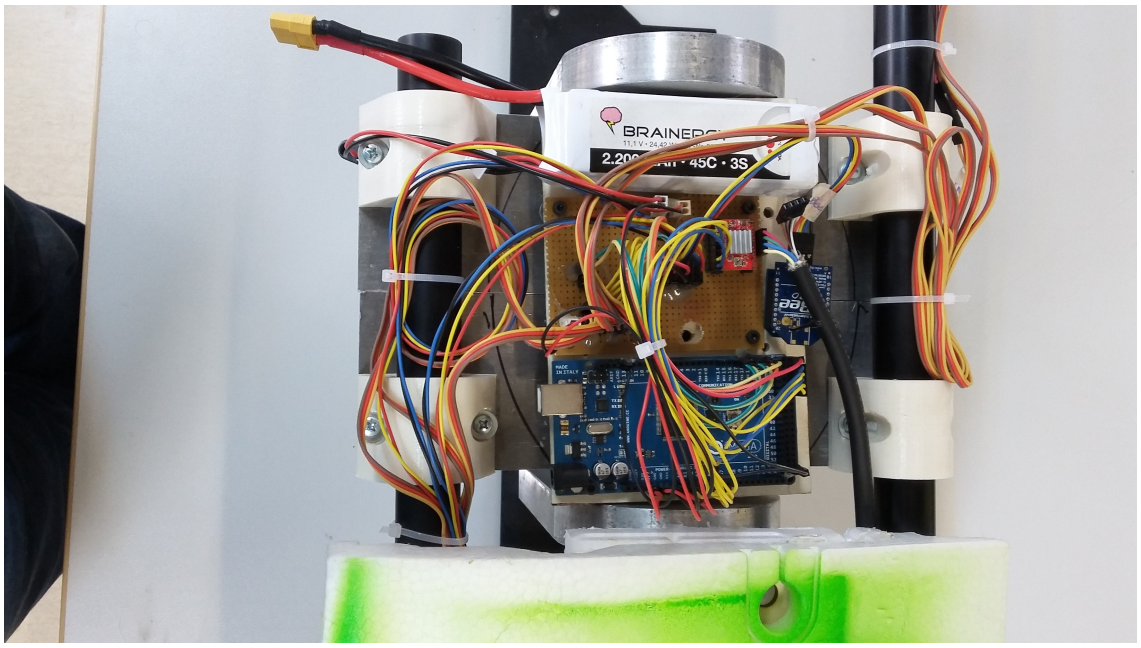

Figure 6.9: Top view of the calibrator control and communication electronics

6.5 LabView data collection program

It was deemed important that sensor measurements from the calibrator would be synchronized with the measurements of the reference differential pressure sensor, in order to make data synchronization and model identification straightforward.

A LabView program was written to interface both with the data acquisition system of the wind tunnel and with the calibrator telemetry in real time. It would gather both data sources and combine them into a single output .csv file (Figures 6.10, 6.11).

The user interface allowed for remote calibrator control and sampling, in multiple modes (i.e. angle control, one sample capturing, sampling profile initialization).

Unfortunately, due to the constraints of the LabView visual programming language and data rate mismatch between measurements sources, a lot of lines on the output file would be truncated, resulting in loss of data. The amount of lost data varied between 10%-15%. While this amount is significant, the remaining data set was large enough for a satisfactory calibration and characterization procedure.

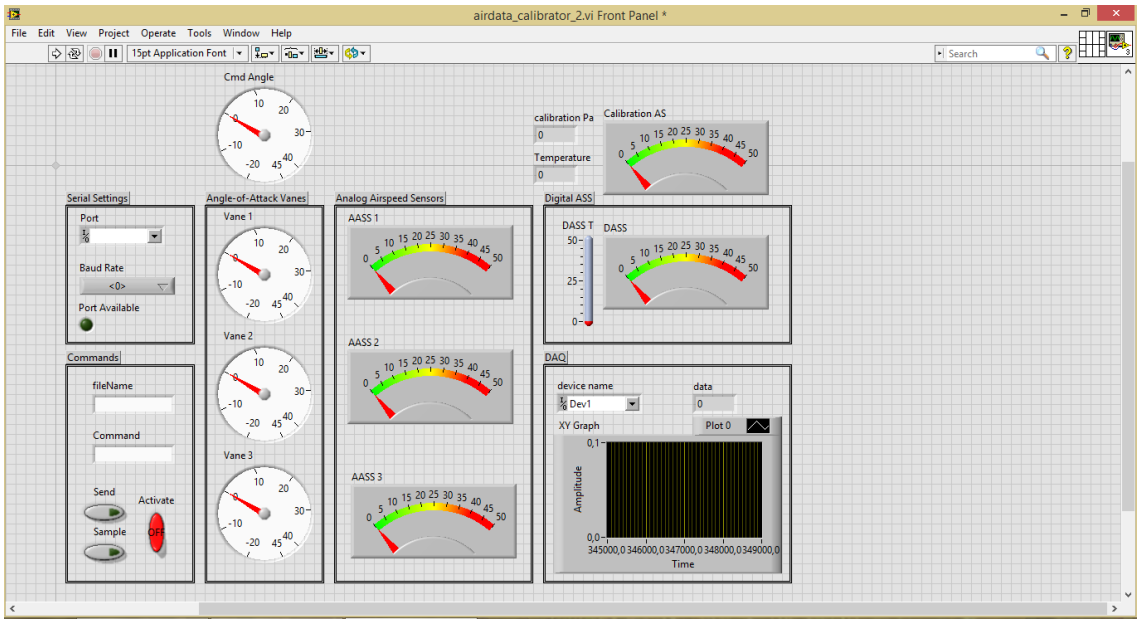

Figure 6.10: Screenshot of the LabView program user interface

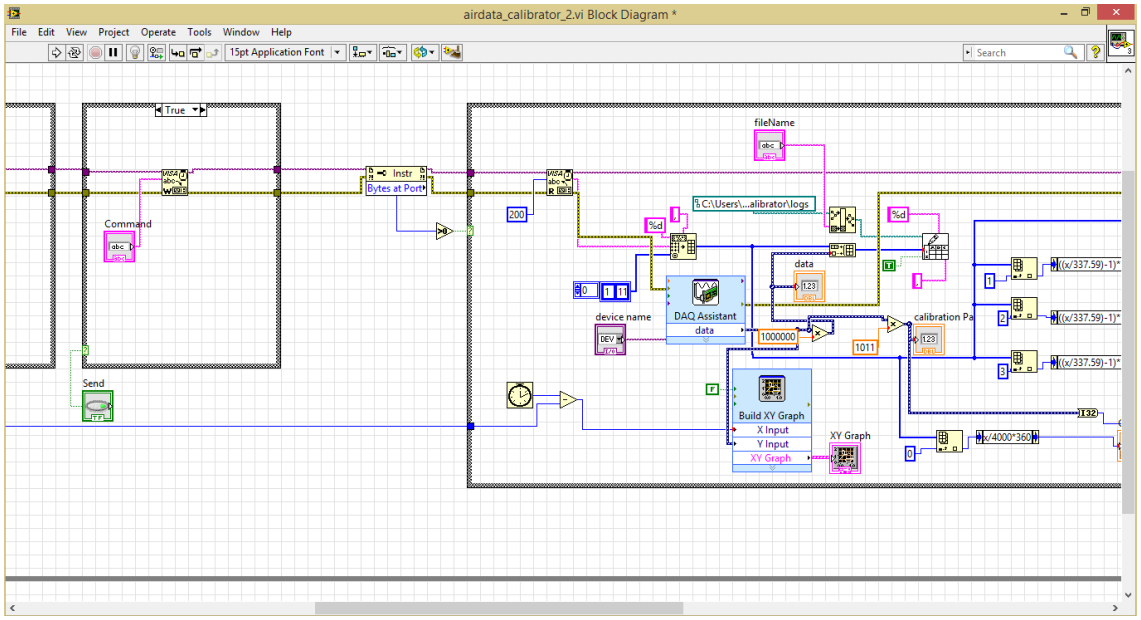

Figure 6.11: Detail of the LabView program visual code

Chapter 7

The Wind Tunnel Facility

7.1 Installation description

The experiments were carried out in the wind tunnel facility of the Laboratory of Aerodynamics, School of Mechanical Engineering, National Technical University of Athens (Figures 7.1, 7.4). The wind tunnel is powered by a 350hp, seven blade axial fan and is a closed flow circuit. The experiments took place in the smallest test section of the installation, out of total three, with dimensions 1.8 m by 1.4 m (w x h) (Figure 7.2).

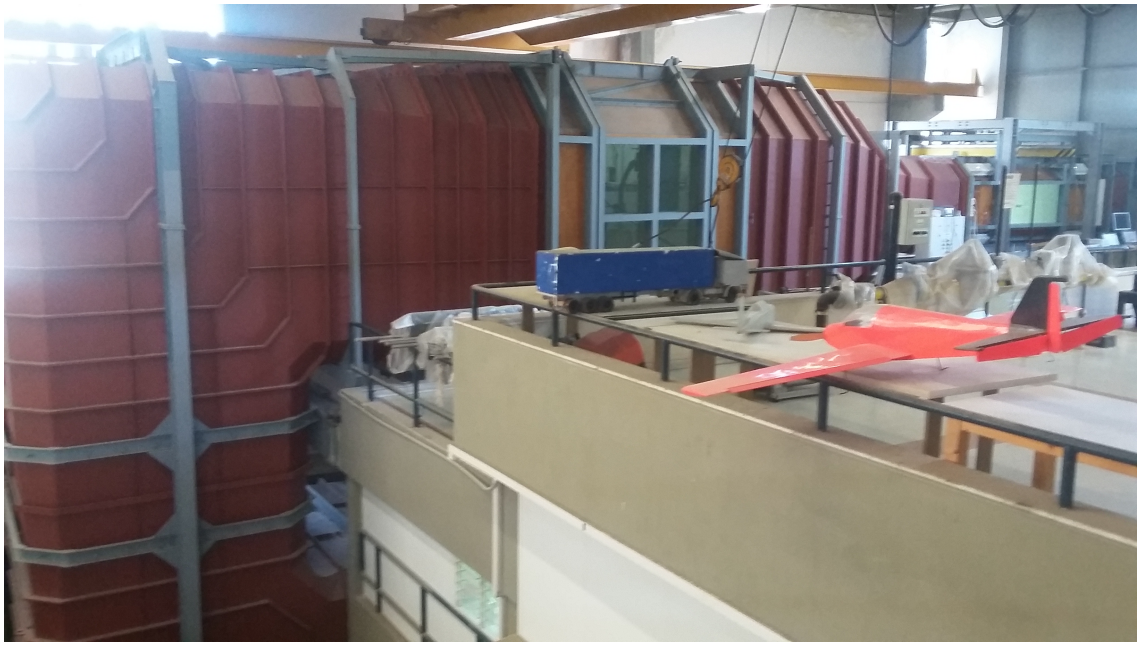

Figure 7.1: The upper floor of the wind tunnel

Figure 7.2: The narrow test section of the upper floor

Figure 7.3: The wide test section the lower floor

Figure 7.4: The exterior section of the wind tunnel

7.2 Reference Instrument

The instrument used to capture reference differential pressure measurements was a Furness FCO16 differential pressure sensor, whose calibration specifications can be seen in Table 7.1. It was connected with silicon tubing to a Pitot-static probe within the wind tunnel.

Measurement Range	$\pm 2000\,\mathrm{Pa}$
Output	Analog Signal
Output Range	$\pm\ 2\,\mathrm{V}$
Scaling coefficient variance	$2.2421\,\mathrm{Pa\,V^{-1}}$
Output variance	$5.1059\,\mathrm{Pa}$

Table 7.1: The reference differential pressure sensor (manometer) specifications

Figure 7.5: The exterior section of the wind tunnel

The output of the reference manometer was connected to the National Instruments NI USB-6251 data acquisition system (Figure 7.6), in turn connected to a computer through a USB interface. The relevant specifications of the DAQ are presented in Table 7.2.

Figure 7.6: The exterior section of the wind tunnel

Analog input range	±10 V,±5 V,±2 V,±1 V,±0.5 V,±0.2 V,±0.1 V,
Resolution	16-bit
Analog input type	Absolute, Differential
Sampling rate	up to 1.25MS/s single channel

Table 7.2: The reference data acquisition system specifications

7.3 Method of control

For each experiment, the desired airspeed value was converted to differential pressure, for a nominal air density value. The wind tunnel fan RPM were controlled with a rotational knob interface, until the reference manometer reading matched the desired differential pressure.

During each experiment, the fan RPM were not controlled to maintain the desired differential pressure; the control input was constant and open-loop.

Chapter 8

Presentation of test runs

Multiple test runs were performed in the span of two days. Different calibrator configurations and wind tunnel settings were used each time. Table 8.2 presents all of the controlled variables for each test, in a digestible format.

Separate tests were run to acquire barometer readings, because the barometer sensor had a significantly slower sampling rate. 1000 samples were captured at 0 degrees of AoA. The barometer tests are listed in Table 8.1.

Test designation	**nominal airspeed** (m/s)	**wing applied?**	**Start time**
bc_0_b	0	N	Day 1 - 18:13
bc_5_b	5	N	Day 1 - 18:16
bc_10_b	10	N	Day 1 - 18:19
bc_15_b	15	N	Day 1 - 18:21
bc_20_b	20	N	Day 1 - 18:23
bc_25_b	25	N	Day 1 - 18:33
bc_30_b	30	N	Day 1 - 18:34
bc_35_b	35	N	Day 1 - 18:36
bc_40_b	40	N	Day 1 - 18:38
bm_0_b	0	N	Day 2 - 10:35
bm_20_b	20	N	Day 2 - 12:24
wc_0_b	0	Y	Day 2 - 12:35
wc_20_b	20	Y	Day 2 - 13:15

Table 8.1: List of barometer tests

Test designation	**nominal airspeed** (m/s)	**wing applied?**	**AoA sweep range (°)**	**AoA sweep step (°)**	**Start time**
bc_0	0	N	−20° to 25°	5	Day 1 - 18:48
bc_5	5	N	−20° to 25°	5	Day 1 - 19:03
bc_10	10	N	−20° to 25°	5	Day 1 - 19:17
bc_15	15	N	−20° to 25°	5	Day 1 - 19:25
bc_20	20	N	−20° to 25°	5	Day 1 - 19:43
bc_25	25	N	−20° to 25°	5	Day 1 - 19:47
bc_30	30	N	−20° to 25°	5	Day 1 - 19:52
bc_35	35	N	−20° to 25°	5	Day 1 - 20:04
bm_0	0	N	−5° to 15°	1	Day 2 - 11:48
bm_5	5	N	−5° to 15°	1	Day 2 - 11:52
bm_10	10	N	−5° to 15°	1	Day 2 - 11:59
bm_15	15	N	−5° to 15°	1	Day 2 - 12:06
bm_20	20	N	−5° to 15°	1	Day 2 - 12:15
wc_0	0	Y	−20° to 25°	5	Day 2 - 12:37
wc_5	5	Y	−20° to 25°	5	Day 2 - 12:42
wc_10	10	Y	−20° to 25°	5	Day 2 - 12:49
wc_15	15	Y	−20° to 25°	5	Day 2 - 12:55
wc_15r	15	Y	−20° to 25°	5	Day 2 - 13:45
wc_20	20	Y	−20° to 25°	5	Day 2 - 13:00
wf_15	15	Y	−5° to 15°	0.5	Day 2 - 13:31
wf_20	20	Y	−5° to 15°	0.5	Day 2 - 13:18

Table 8.2: List of test runs

Chapter 9

Calibration of AoA and AoS sensing systems

In this chapter, we shall present the calibration model for the AoA and AoS sensing systems, termed *AoA sensors* for the rest of the chapter, since their mode of operation is identical in AoA and AoS scenarios. The accuracy of the model was characterized and the model validated against a time series separate from the calibration data set.

9.1 Calibration on the full test range

Calibration Data

The data sets which were used for the calibration procedure were

- bm_10, bm_15, bm_20
- wf_15, wf_20

For each AoA sensor, the relevant regressors and measurements were isolated, so that each sensor could be calibrated separately.

The time series of each calibration data set were concatenated into a single data set, so that all available information could be processed at once, increasing the sample number for a single characterization procedure.

Ordinary Least Squares were used to perform model fitting.

Regressor Selection

The available relevant regressors for the model fitting were bias offset 1, airspeed V_a, reference angle α_r, squared reference angle α_r^2 and αV_a.

Upon preliminary inspection, the regressors 1 and α_r were the ones selected as having significant contribution, resulting in the calibration model

$$\alpha_i = \theta_0 + \theta_\alpha \alpha_r \tag{9.1}$$

Parameter extraction - AoA sensor 1

A sample time series of α_r and α_1 can be seen in the following Figure 9.1. It is evident that the measured quantity diverges significantly from the actual AoA, hence a calibration procedure is justified.

The resulting calibration coefficients are presented in Table 9.1.

The model fit and fit error plots can be seen in Figure 9.2.

Parameter extraction - AoA sensor 2

Similarly to the previous subsection, time series of α_r and α_1 can be seen in the Figure 9.3. This vane appeared to be "stuck" in parts of the experiment where the airspeed was low. These parts were discarded from the calibration procedure but it was noted that this sensor exhibited greater shaft friction.

The resulting calibration coefficients are presented in Table 9.2

The model fit and fit error plots can be seen in Figure 9.4.

Parameter extraction - AoA sensor 3

Finally, sample time series of α_r and α_1 can be seen in the following figure 9.5.

The resulting calibration coefficients are presented in Table 9.3

The model fit and fitting error plot can be seen in Figure 9.6.

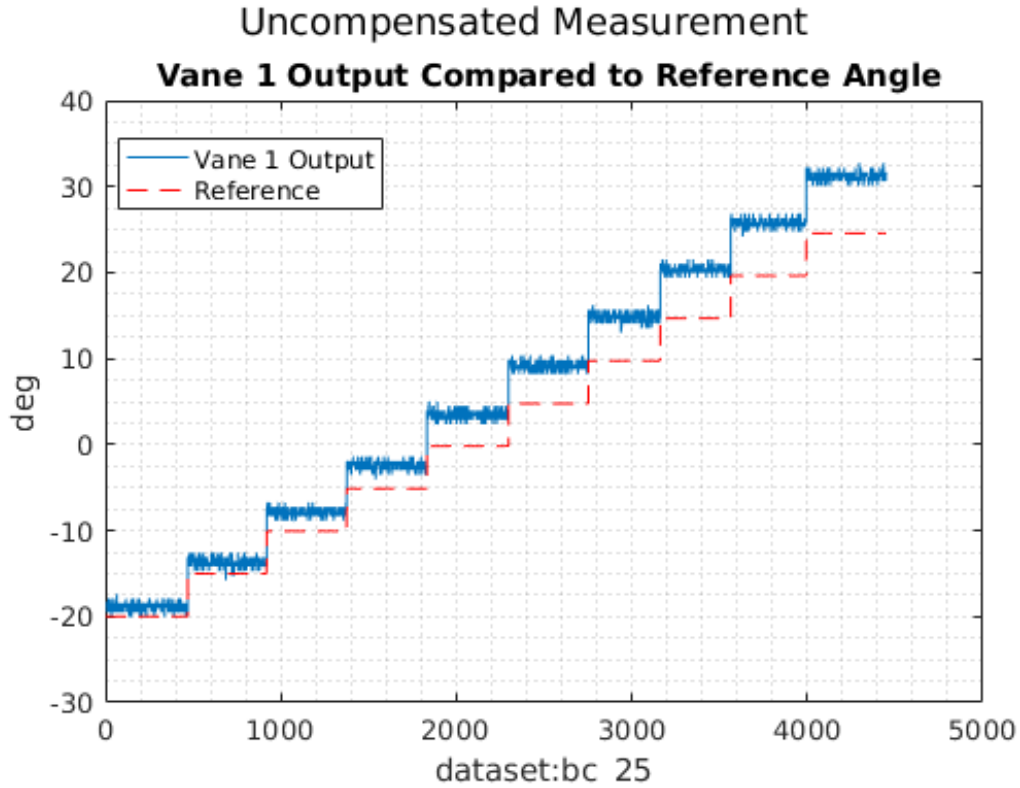

Figure 9.1: Comparison between AoA sensor 1 output & reference output

AoA sensor 1 identification (full AoA range)		
Parameter name	**Parameter value**	**Error bounds (95% - white)**
θ_0	3.9017	$\pm$0.0054
θ_α	1.1370	$\pm$0.0007
R^2	0.9923	

Table 9.1: AoA sensor 1 calibration coefficients

AoA sensor 2 identification (full AoA range)		
Parameter name	**Parameter value**	**Error bounds (95% - white)**
θ_0	4.2905	$\pm$0.0056
θ_α	0.9518	$\pm$0.0018
R^2	0.9898	

Table 9.2: AoA sensor 2 calibration coefficients

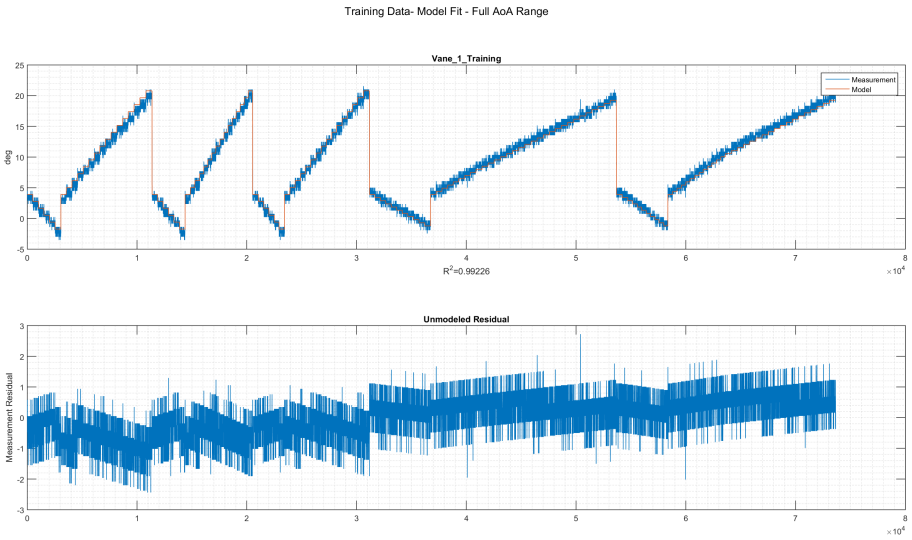

Figure 9.2: Model training for AoA sensor 1

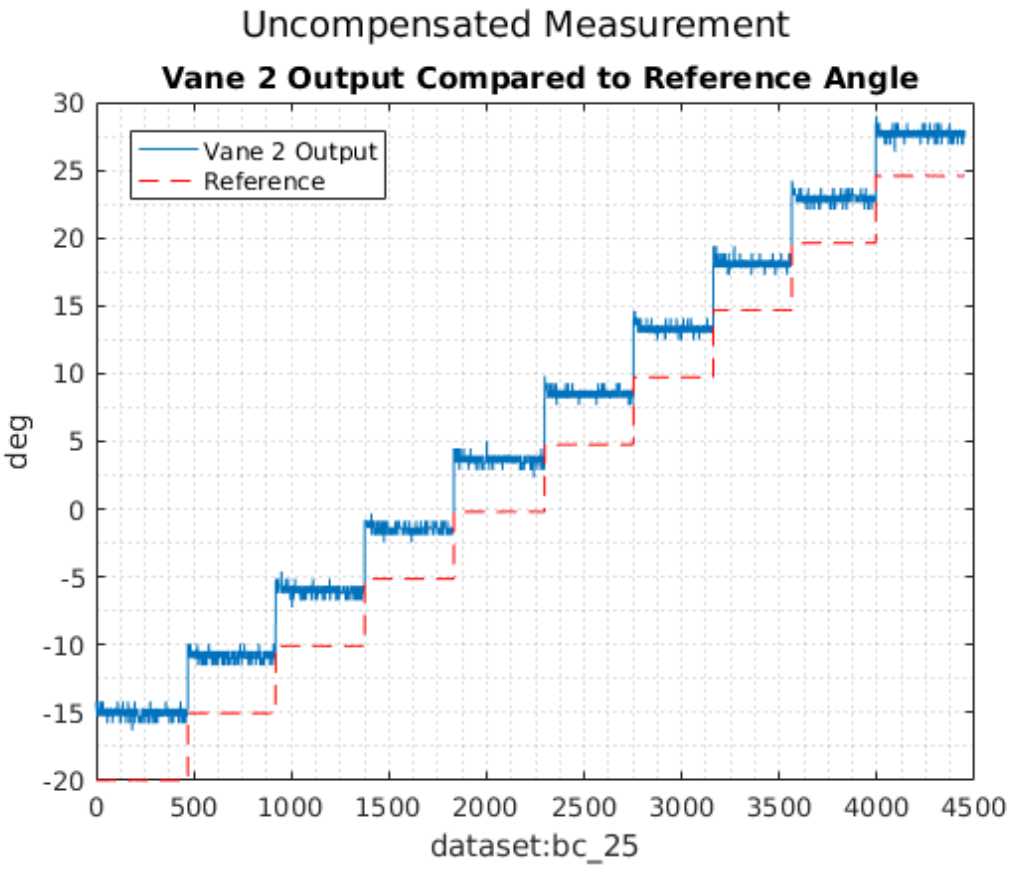

Figure 9.3: Comparison Between Vane & Reference Outputs

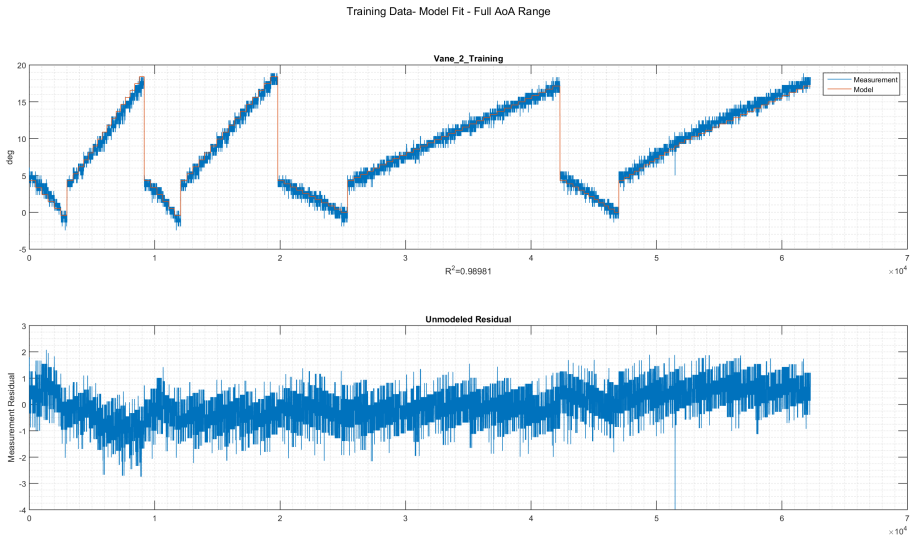

Figure 9.4: Model training for AoA sensor 2

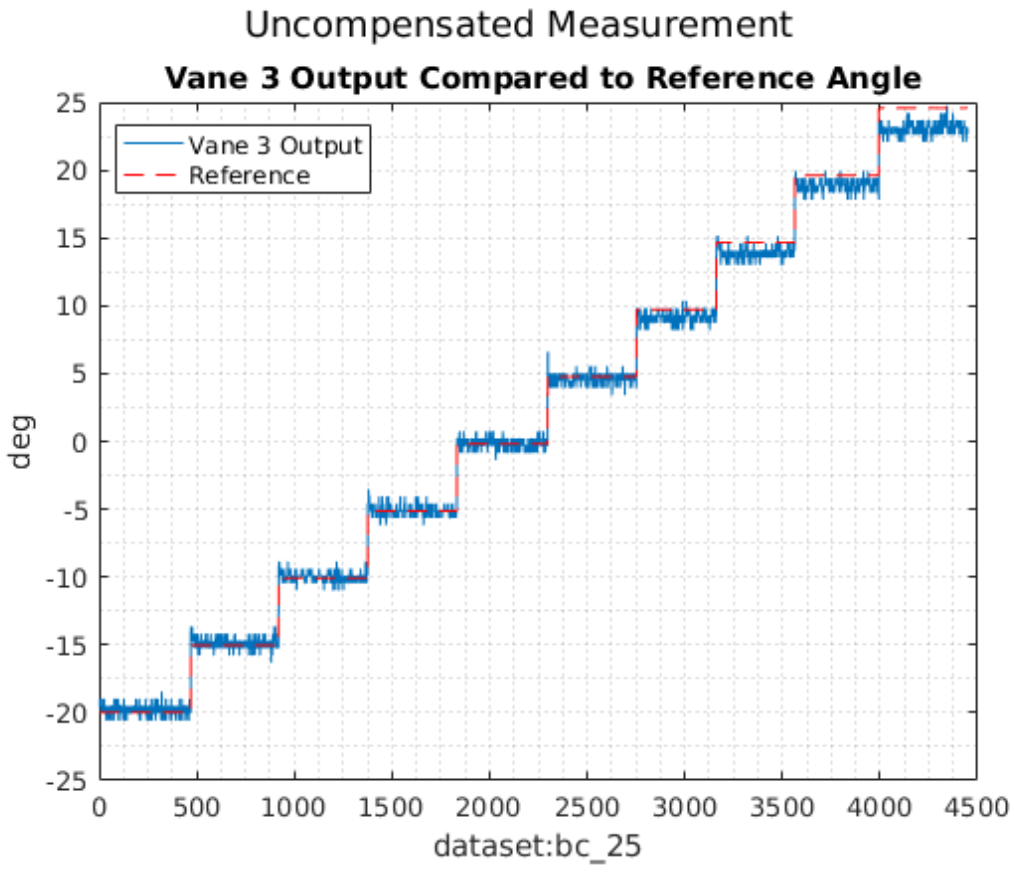

Figure 9.5: Comparison Between Vane & Reference Outputs

AoA sensor 3 identification (full AoA range)		
Parameter name	**Parameter value**	**Error bounds (95% - white)**
θ_0	0.6730	± 0.0052
θ_α	0.9760	± 0.006
R^2	0.9902	

Table 9.3: AoA sensor 3 calibration coefficients

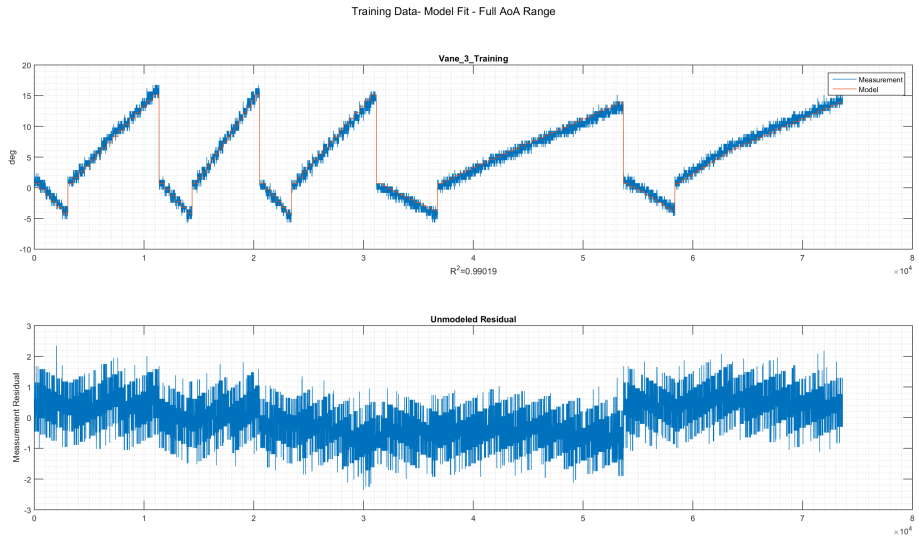

Figure 9.6: Model training for AoA sensor 3

9.2 Validation Data

The data sets which were used for the validation procedure were

- bc_10, bc_15, bc_20, bc_25, bc_30, bc_35
- wc_10, wc_15, wc_15_repeat, wc_20

It is important to state the assumption that placement of the wing does not affect the readings of the AoA sensors.

Validation of the vane models

The plots of the estimated sensor output versus the actual outputs and the estimation error of each sensor can be seen in Figures 9.7, 9.8 and 9.9. The error statistics for all three sensors can be seen in Table 9.4.

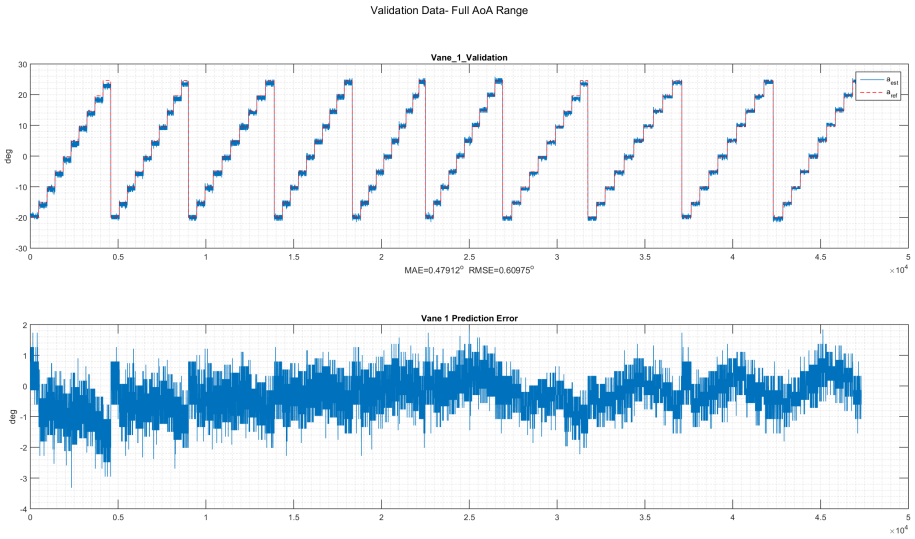

Figure 9.7: Model validation for AoA sensor 1

AoA sensors model validation - full range			
Error Metric	Sensor 1	Sensor 2	Sensor 3
MAE (deg)	0.54437	0.65930	0.7477
RMSE (deg)	0.68751	0.90803	0.89947

Table 9.4: AoA sensor validation error statistics

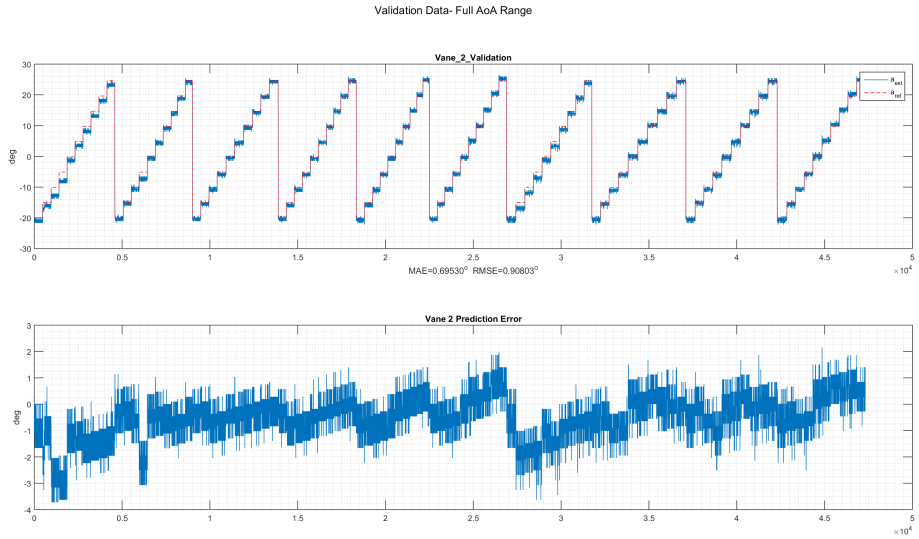

Figure 9.8: Model validation for AoA sensor 2

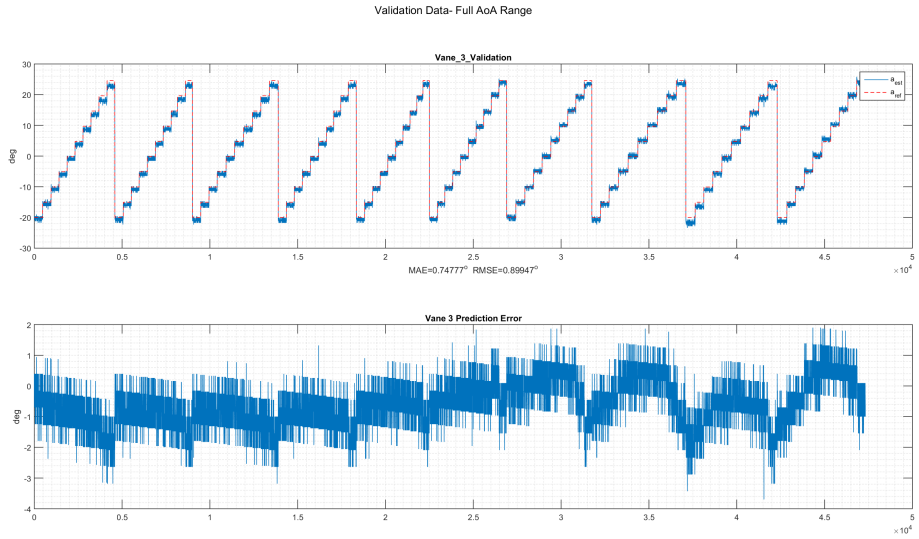

Figure 9.9: Model validation for AoA sensor 3

9.3 Calibration on the nominal AoA range

Parameter extraction - Reduced envelope

Even though the results are definitely usable, it was deemed worthwhile to repeat the validation procedure over the nominal range of the flight envelope, which we specify as $\alpha_r \in [-5, 15]\,^\circ$. As most mid-range UAVs operate under this envelope, the following analysis was narrowed down so as to determine the error on this specific area. No changes have been applied to the calibration procedure or the identified coefficients.

Validation of the vane models - Reduced envelope

Similarly to the full α range test, the plot of the estimated sensor output versus the actual reference AoA can be seen in Figures 9.10, 9.11 and 9.12. The error statistics for all three sensors can be seen in Table 9.5.

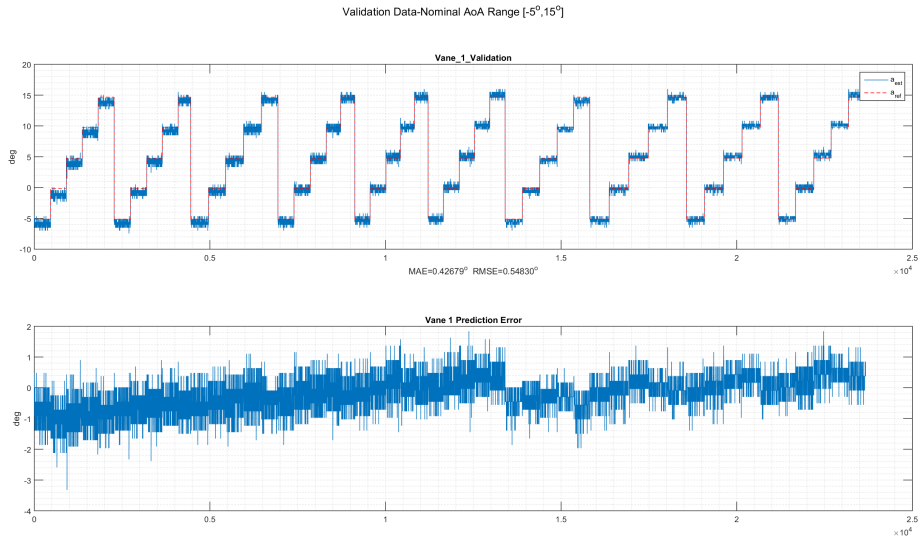

Figure 9.10: Model validation for AoA sensor 1 - Nominal envelope

AoA sensors model validation - nominal AoA range			
Error Metric	Sensor 1	Sensor 2	Sensor 3
MAE (deg)	0.42679	0.70464	0.63591
RMSE (deg)	0.54380	0.94537	0.75422

Table 9.5: AoA sensors validation error statistics over the reduced α range

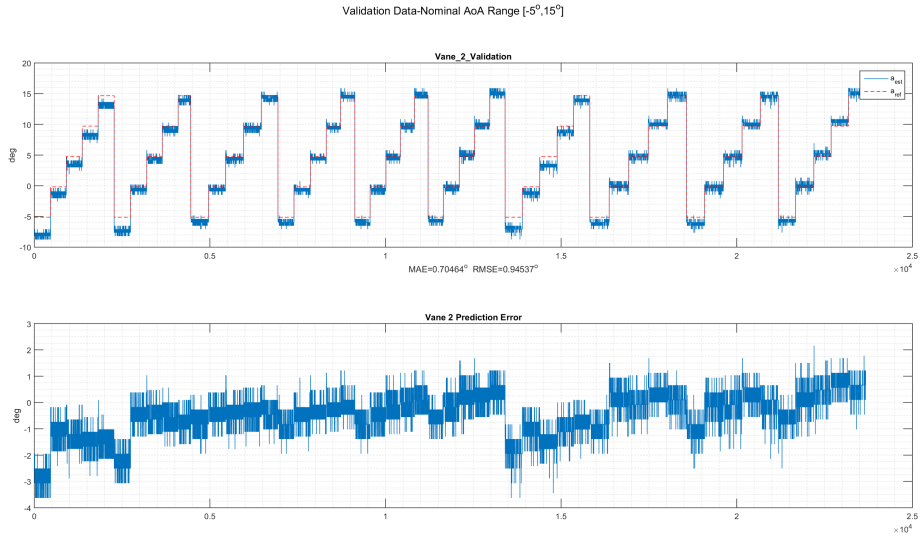

Figure 9.11: Model validation for AoA sensor 2 - Nominal envelope

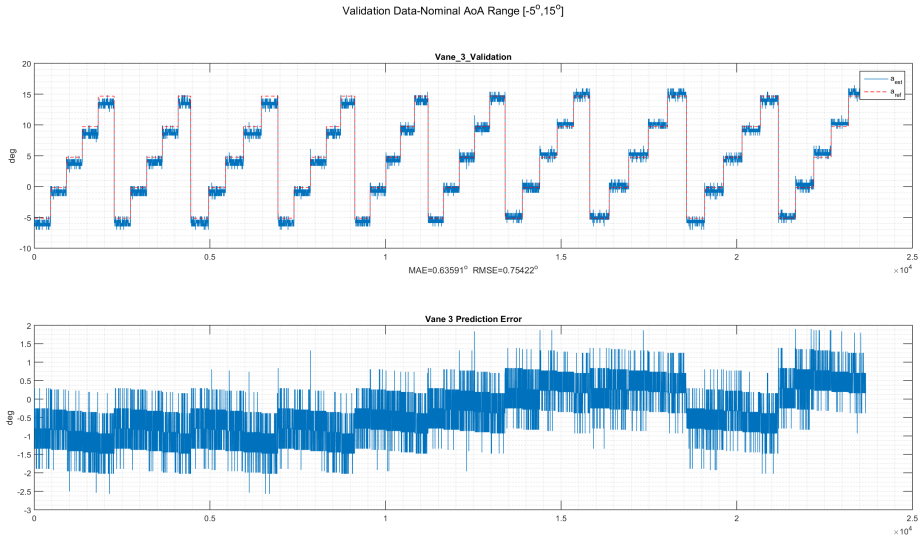

Figure 9.12: Model validation for AoA sensor 3 - Nominal envelope

Chapter 10

Calibration of the Pitot-static Probes

In this chapter the calibration procedures for the Pitot-static probes will be presented. In order to have directly comparable results and linear error models, the investigation is performed in the domain of differential pressure, instead of airspeed. The main focus is to:

1. Produce calibration models for the airspeed sensors 1 and 2 without a wing installed, so that a benchmark performance is established.
2. Compare the performance of airspeed sensors 2 and 3 without a wing installed, to highlight the impact of the MS4525DO.
3. Compare the performance of airspeed sensors 1 and 2 when a wing is installed and make compensation efforts if required.
4. Discuss the error statistics during conversion from differential pressure to airspeed.

Airspeed sensor 4 incorporated a Pitot-static probe with malformed nosecone. Its measurements were completely unsalvageable, hence it was not included in this analysis.

Data Partitioning

Regression techniques such as Ordinary Least Squares (OLS) require a training data set in order to compute the model coefficients. Validation data is then applied to the computed models for reliability assessment. The latter procedure, makes use of reference values which are considered to be the best available estimate of the variables-to-be-explained.

Each group of data must be evaluated using appropriate statistical metrics. The ability of the model to fit in the training data will be characterized with the use of the coefficient of determination (R^2). Though frequently criticized for its inability to account for model over-parameterization and predictability, R^2 is considered as a sufficient metric when validation is part of the overall procedure. After training, the extracted models are reversed (so as to isolate the quantity of interest) and validation data is used to obtain estimates of the differential pressure. These estimates are then compared to reference values, and errors are analyzed using the Mean Absolute Error (MAE) and the Root Mean Squared Error (RMSE). Errors were also tested for normality (using Kolomogorov Smirnoff & Lilliefor's tests)- although the null hypothesis was rejected in all cases.

Consequently, one must decide how to divide the available data into training and validation groups. As no repeated experiments (under identical conditions) were conducted, we decided to divide the very same datasets into two subsets. The structure of the obtained data made this a convenient choice as the states of the sensor were of discrete nature (regarding AoA, differential pressure), conducted in constant steps each of which had a large number of samples. Hence, the first half of the samples of each state was assigned to the data training set while the second half to the validation set.

The data sets used for the calibration procedure without a wing were:

- bc_5, bc_10, bc_15, bc_20, bc_25, bc_30, bc_35
- bm_5, bm_10, bm_15, bm_20

The datasets used for the calibration with the wing installed were:

- wc_5, wc_10, wc_15, wc_15_repeat
- wf_15, wf_20

10.1 Calibration without a wing

Two calibration efforts have been performed. The first intends to characterize the measurements over a small range of AoA, namely $\alpha \in [-5, 15]\,^\circ$, which is typical of most fixed-wing aircraft. The second extends the AoA range to the full available $\alpha \in [-20, 25]\,^\circ$, to investigate sensor performance on extreme angles of attack. This gains more importance gradually, along with the emergence of hybrid aircraft which are able to transition from and to the stall regime.

As in the AoA sensor calibration, data series relevant to each sensor were isolated and examined separately.

Calibration on the reduced AoA range

The range $\alpha \in [-5, 15]^\circ$ is the most common flight envelope on standard fixed-wing aircraft configurations. The initial differential pressure measurement time series for sensors 1, 2 and 3 against the known quantity (in both nominal and extended ranges) can be seen in Figures 10.1 and 10.2. In these figures, the measurement offset from each sensor is removed and the resulting (otherwise uncompensated) sensor output is plotted.

It is trivial to calculate the sensor bias, by averaging an output window on zero input (covered Pitot-static sensor), and indeed most autopilot systems employ this technique during system initialization. Thus, we removed the offset from these measurements to set a benchmark for the calibration and compensation procedure which follows.

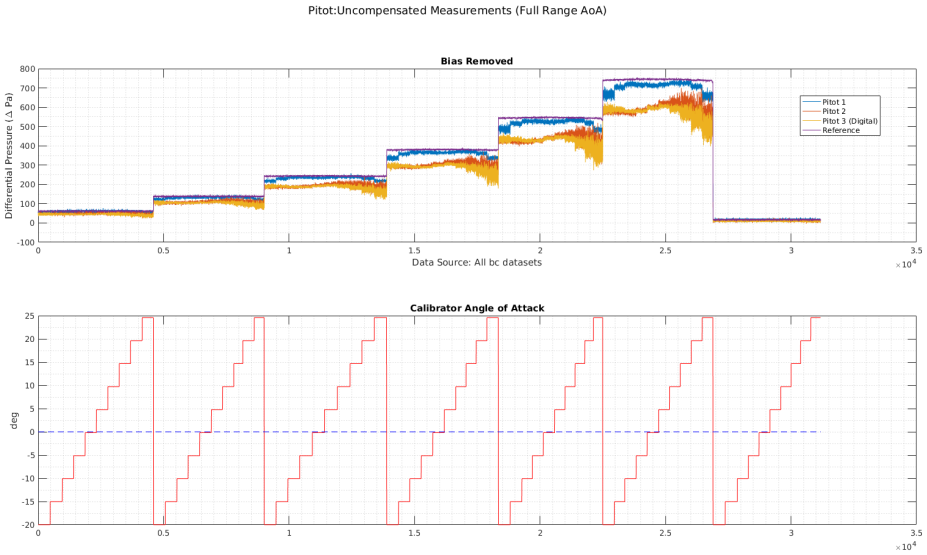

Figure 10.1: Uncompensated measurements - full AoA range

The error statistics for these measurements are shown in Tables 10.1 and 10.2. MAE refers to the Mean Average Error while RMSE to the Root-Mean-Square error.

instrument	sensor 1	sensor 2	sensor 3
MAE (Pa)	16.22	63.78	71.71
RMSE (Pa)	23.74	82.82	92.06

Table 10.1: Pitot probes uncalibrated error statistics in full AoA range (bias eliminated)

The error is very large and the effect of both airspeed and AoA is immediately noticeable on the plotted data series.

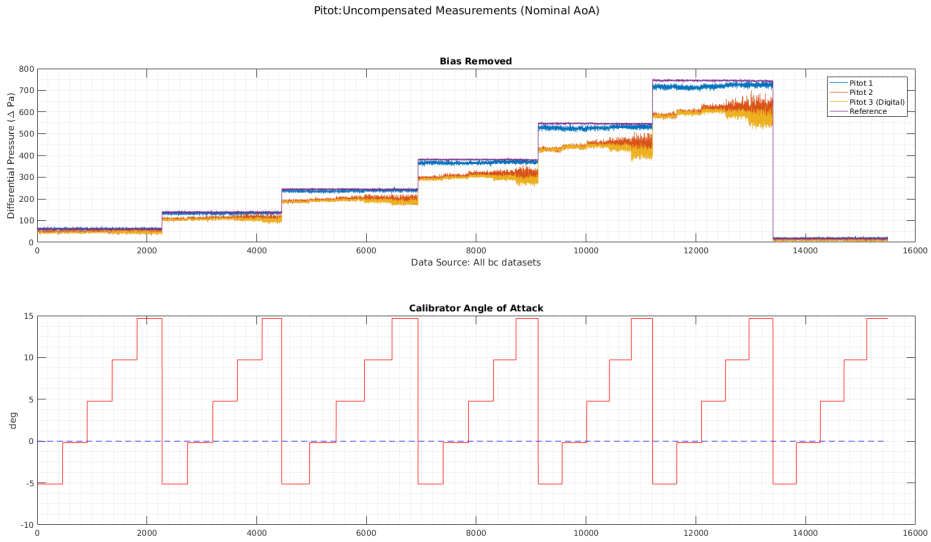

Figure 10.2: Uncompensated measurements - nominal AoA range

instrument	sensor 1	sensor 2	sensor 3
MAE (Pa)	14.51	61.62	70.01
RMSE (Pa)	21.15	79.94	89.47

Table 10.2: Pitot probes uncalibrated error statistics in the nominal AoA range (bias eliminated)

Proceeding with the calibration, the initial regressor pool is $\{P_{d,r}, abs(\alpha)P_{d,r}, \alpha^2 P_{d,r}\}$. A bias term is not considered, since measurement offset is already compensated. The reason why $abs(\alpha)$ is selected instead of α is that the contribution of α on the measured differential pressure is negative (decreasing), regardless of its sign, i.e. in positive or negative AoA.

After a thorough investigation we concluded that, under nominal AoA ranges, the contribution of α might as well be ignored for the sake of a simpler sensor model. Thus,only $P_{d,r}$ was included in the regressor pool for this leg of the experiment. The resulting regressor coefficients can be seen in Table 10.3.

instrument	$\theta_{P_{d,r}}$	R^2
sensor 1	0.9670 $\pm$0.0001	0.9991
sensor 2	0.8100 $\pm$0.0002	0.9967
sensor 3	0.7826 $\pm$0.0002	0.9973

Table 10.3: Probe coefficients on reduced α range

The time series of the measurement versus the model output and the model error

for each probe can be seen in Figures 10.3, 10.4 and 10.5.

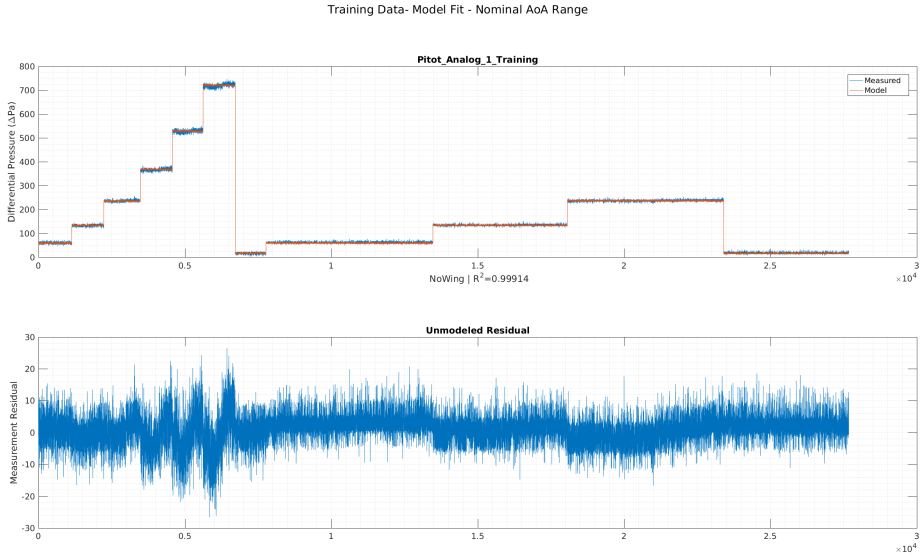

Figure 10.3: Model training for airspeed sensor 1 - Nominal AoA range

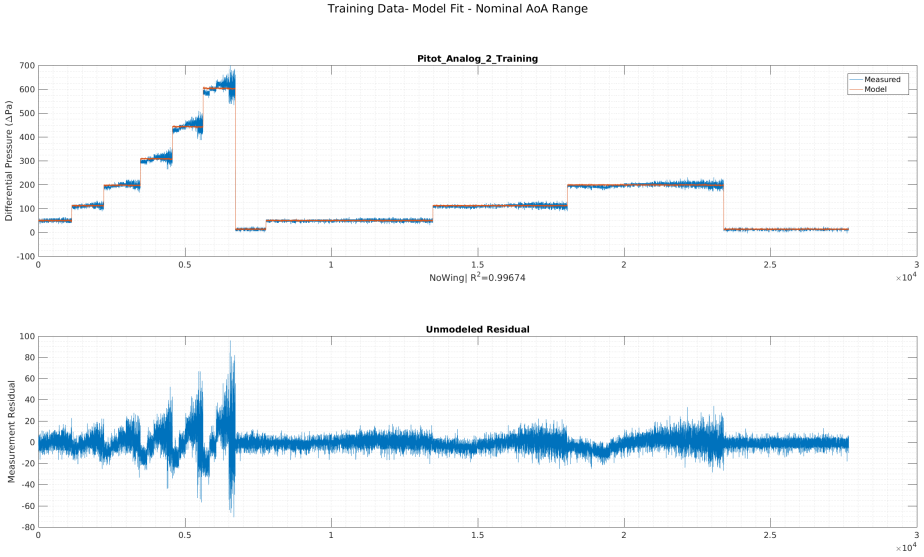

Figure 10.4: Model training for airspeed sensor 2 - Nominal AoA range

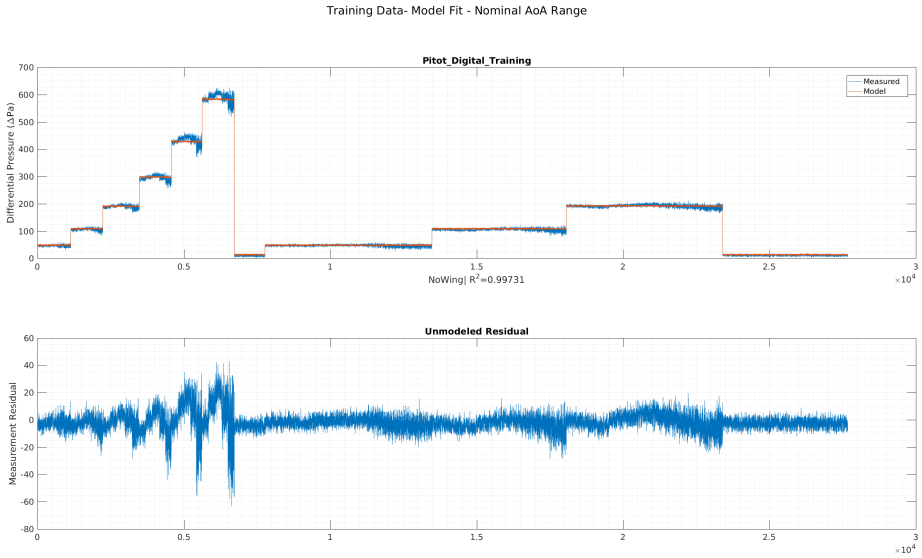

Figure 10.5: Model training for airspeed sensor 3 - Nominal AoA range

The prediction error for each probe model, when applied on the validation data set, can be seen in Figures 10.6, 10.7 and 10.8 while the error statistics are shown in Table 10.4.

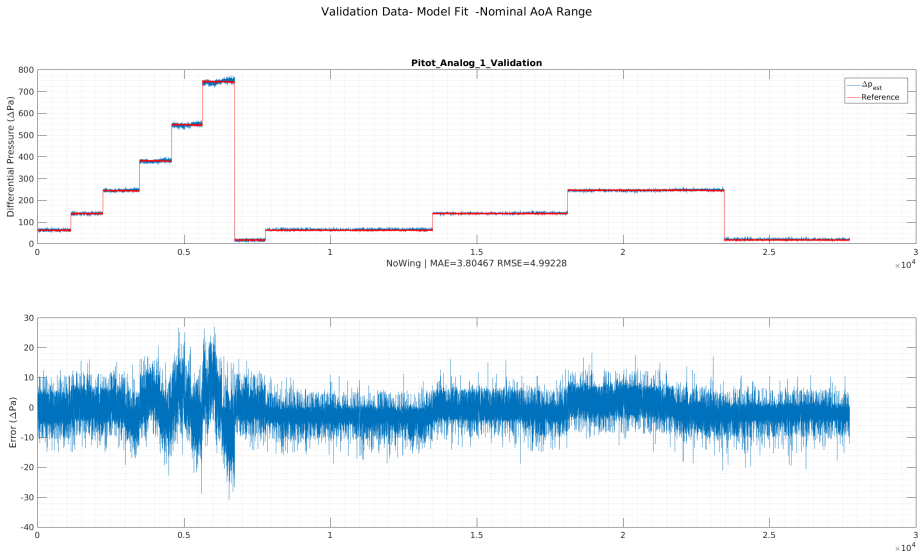

Figure 10.6: Model validation for airspeed sensor 1 - Nominal AoA range

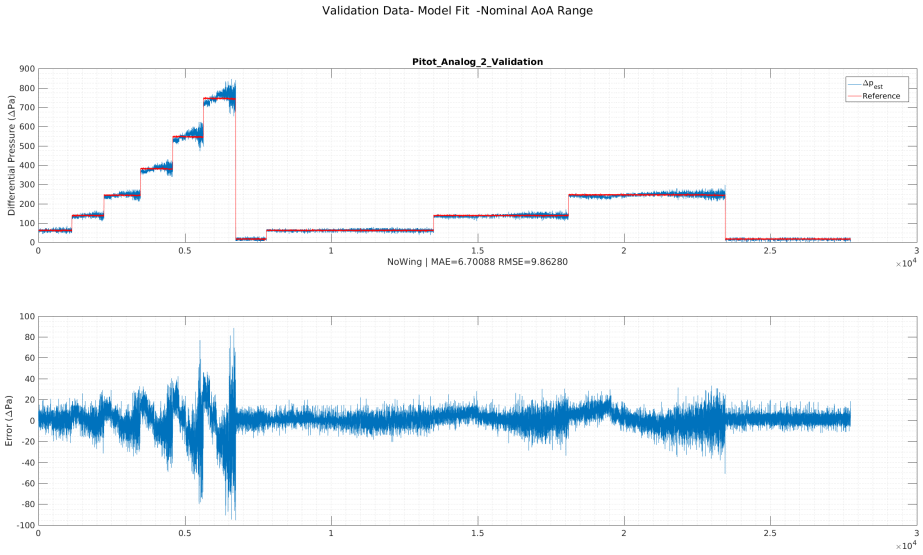

Figure 10.7: Model validation for airspeed sensor 2 - Nominal AoA range

Instrument	sensor 1	sensor 2	sensor 3
MAE (Pa)	3.8047	6.7009	6.4057
RMSE (Pa)	4.9923	9.8628	8.9747

Table 10.4: Probes 1, 2 & 3: Prediction error statistics - Nominal AoA range

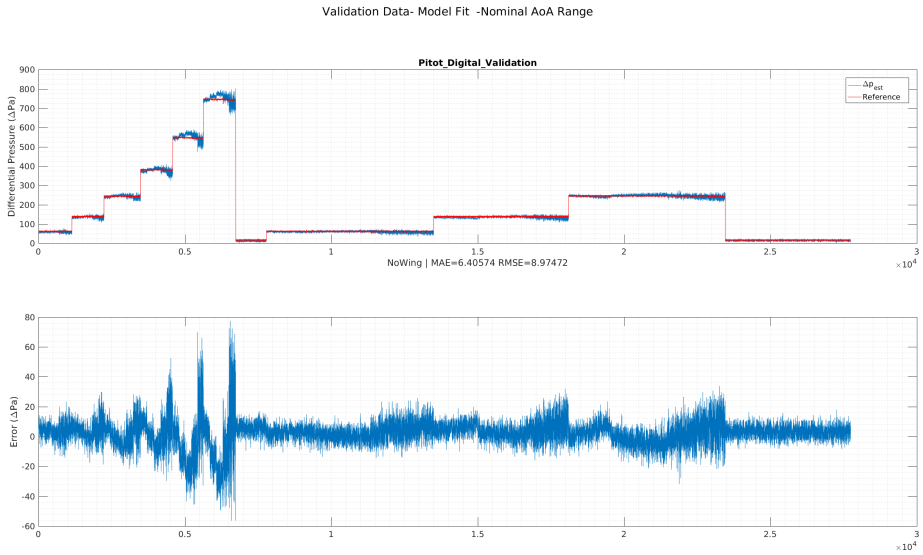

Figure 10.8: Model validation for airspeed sensor 3 - Nominal AoA range

Calibration on the full AoA range

As mentioned in the beginning of the chapter, there is an increasing number of hybrid aircraft, which are able to fly in flight modes other than this of the traditional airplane. Fixed-wing VTOLs [4] and hybrid flying wings [2] are able to transition their flight mode past the stall boundary and then return back to normal flight. For this kind of vehicles it is valuable to have an accuracy estimate of the airspeed reading during flight mode transition.

For that reason, a probe investigation was also carried out for the full $\alpha \in [-20, 25]^\circ$ range which was available from the experiment. The data sets used for this observation are the same as previously, but using the extended AoA range.

Initially, let us observe that in high AoA the absolute measurement error of the probe becomes significant, as displayed in Figure 10.9. Thus, the contribution of AoA is no longer small in the AoA range of interest.

Using the regressor pool $\{P_{d,r}, abs(\alpha)P_{d,r}, \alpha^2 P_{d,r}\}$ we end up with the following model:

$$z = P_{d,r}(\theta_0 + \theta_1|\alpha| + \theta_2\alpha^2)$$

The new calibration coefficients can be seen in Table 10.5, while the maximum contribution of each regressor is listed in Table 10.7. Output and fit error are displayed in Figures 10.10, 10.11 and 10.12. Statistical metrics on the errors can be seen in Table 10.6

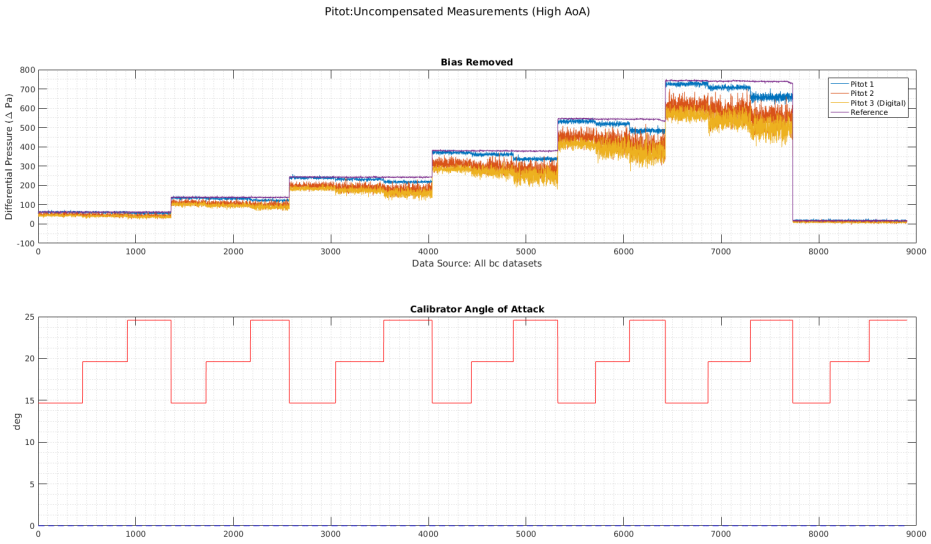

Figure 10.9: Uncompensated Measurements in extreme AoA

With the effect of AoA on measured differential pressure quantified, one can now compensate readings taken on high AoA. However, the increase in measurement variance for high α is noteworthy. This may be attributed to two facts.

instrument	θ_0	θ_1	θ_2	R^2
sensor 1	0.9523 $\pm 2.97 \cdot 10^{-4}$	0.049 $\pm 5.76 \cdot 10^{-5}$	-0.00031 $\pm 3.91 \cdot 10^{-6}$	0.9988
sensor 2	0.7963 $\pm 5.02 \cdot 10^{-4}$	0.003 $\pm 9.70 \cdot 10^{-5}$	-0.00021 $\pm 3.91 \cdot 10^{-6}$	0.9955
sensor 3	0.7809 $\pm 4.86 \cdot 10^{-4}$	0.038 $\pm 9.39 \cdot 10^{-5}$	-0.00030 $\pm 3.78 \cdot 10^{-6}$	0.9955

Table 10.5: Probe coefficients on full α range

instrument	$\theta_0 P_{d,r}$	$\theta_1 \lvert\alpha\rvert P_{d,r}$	$\theta_2 \alpha.^2 P_{d,r}$
sensor 1	719.21	90.56	139.77
sensor 2	601.42	54.61	92.50
sensor 3	589.76	68.90	135.18

Table 10.6: Maximum Regressor Contribution in (Pa) on full α range

Instrument	sensor 1	sensor 2	sensor 3
MAE (Pa)	4.7006	8.4332	8.6530
RMSE (Pa)	6.7832	13.7502	14.1424

Table 10.7: Probes 1, 2 & 3: Prediction error statistics - Full AoA range

First, the non-ideal probe head design, having sharp edges, may lead to non-laminar flow over the total and static ports earlier than the BAD8mmESP probe. This turbulence will appear as measurement noise.

Second, the design of the probe mounting structure, including the aluminium tube, clamp and wooden plate is non-ideal from an aerodynamics standpoint. Turbulent, non-laminar flow is likely to extend forward of the structure. The shorter length of sensor 2 may place it inside the turbulence field.

This is the first indication that the geometric design of the probe of sensor 1 is clearly superior to sensors 2 and 3.

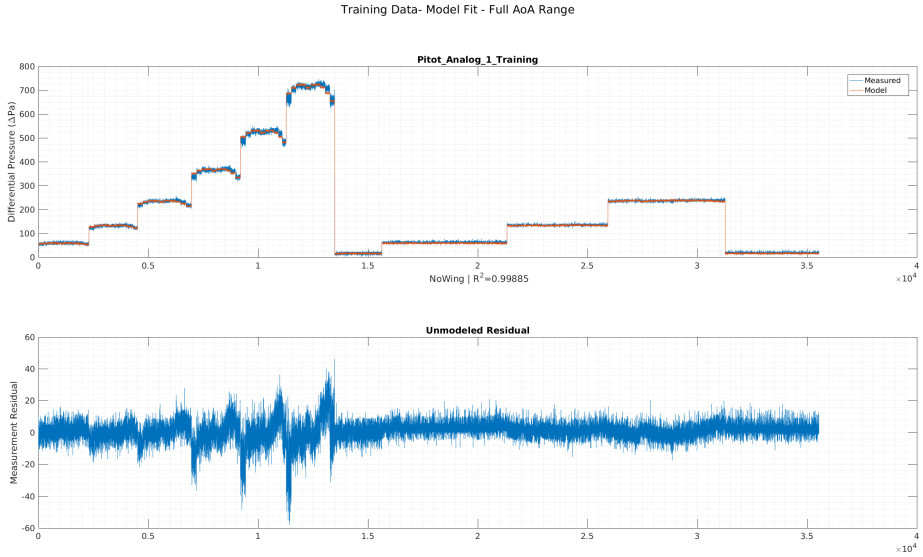

Figure 10.10: Model training for airspeed sensor 1 - Full AoA range

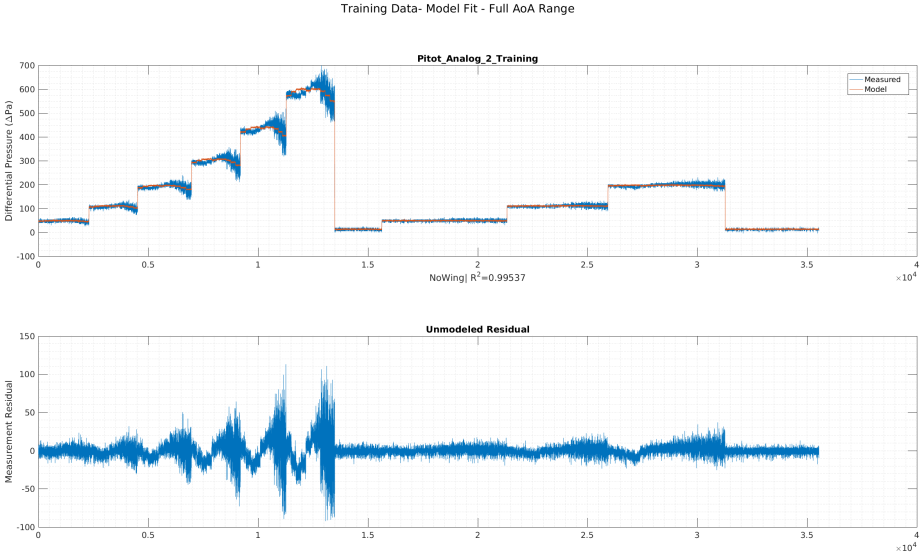

Figure 10.11: Model training for airspeed sensor 2 - Full AoA range

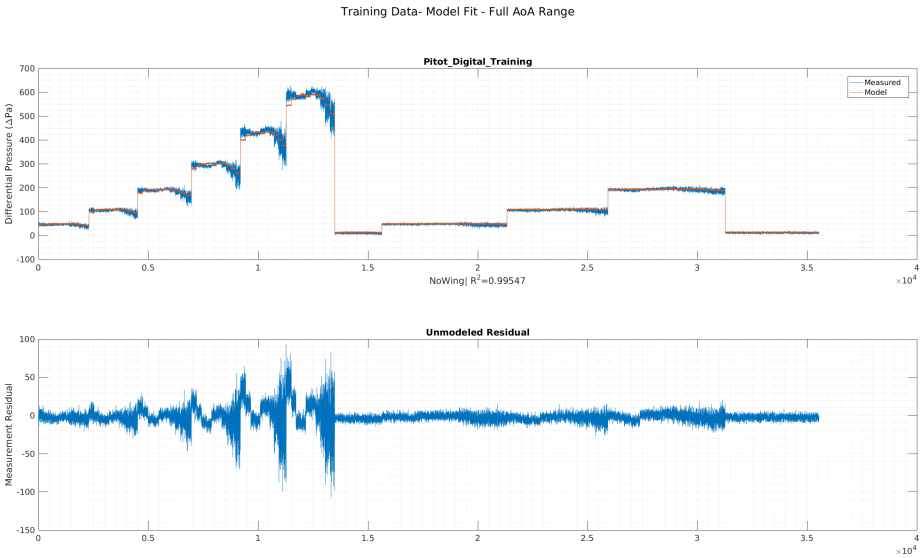

Figure 10.12: Model training for airspeed sensor 3 - Full AoA range

10.2 Digital differential pressure sensor error characteristics

The MS4525DO-DS5AI001D digital differential pressure sensor has gained a lot of popularity and use in the past years in the low-grade UAV community, as a more reliable and accurate sensor for airspeed measurement. Indeed, compared to the older MPXV7002, it has some lucrative features.

Primarily, it has a digital I^2C interface, compared to the analog output voltage of the former. This make it less susceptible to electromagnetic interference, which is always a factor in flying platforms of constrained size. Also it removes the need for an ADC circuit on the interfacing microcontroller; the ADCs found on the microcontrollers are usually of poor resolution (commonly 10 bits) which is a bottleneck on the overall system accuracy.

Additionally, the overall measurement range is $\pm 1\,\text{psi}$=$6894\,\text{Pa}$, greater than that of the MPXV7002, which reaches $\pm 2000\,\text{Pa}$, allowing it to measure airspeeds up to approximately $270\,\text{km}\,\text{h}^{-1}$.

Also, it has a 14-bit ADC, allowing for higher measurement resolution.

However, even though this sounds as an overall upgrade, the impact of the increased resolution on the ADC is not that significant, because of the non-linear relation between airspeed and differential pressure.

$$\Delta P = \frac{1}{2}\rho V_a^2 \tag{10.1}$$

Inverting the above relation for airspeed we get

$$V_a = \sqrt{\frac{2\Delta P}{\rho}} \tag{10.2}$$

Let us run a numerical investigation on the error bounds of both sensors, when converting differential pressure to airspeed, for a range of airspeeds of $V_a = [0, 30]\,\text{m}\,\text{s}^{-1}$. The three data sets seen in Figure 10.13 depict the **maximum** quantization error for the MPXV7002 sampled with 10-bit and 12-bit ADCs and the MS4525DO.

Still, the actual differential pressure error is expected to be much greater for all sensors, so this should be taken into account as well. We have extracted error bounds for both airspeed sensors 2 and 3 in the first section, both uncalibrated and calibrated, over the nominal AoA range. These results were presented in Tables 10.2 and 10.4.

With these error budgets at hand, we can re-calculate the airspeed error. The results are depicted in Figure 10.14. It should be noted that the MPXV7002 was sampled with a 10-bit ADC in all test runs.

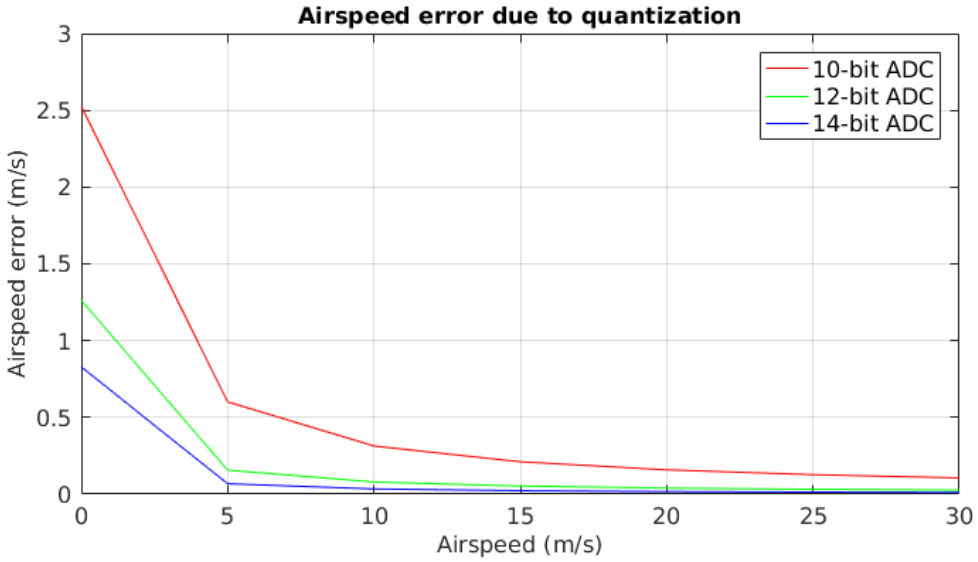

Figure 10.13: Airspeed error due to measurement quantization

In conclusion, even though MS4525DO has a greater relative resolution over its full range span, the increased range greatly reduces the gain in resolution. The arguments for the integrated ADC and digital interface still stand though. Airspeed sensor 3 is only approximately 15% better than airspeed sensor 2, a result which alludes that the Pitot probe design and location plays a great role in airspeed measurement errors.

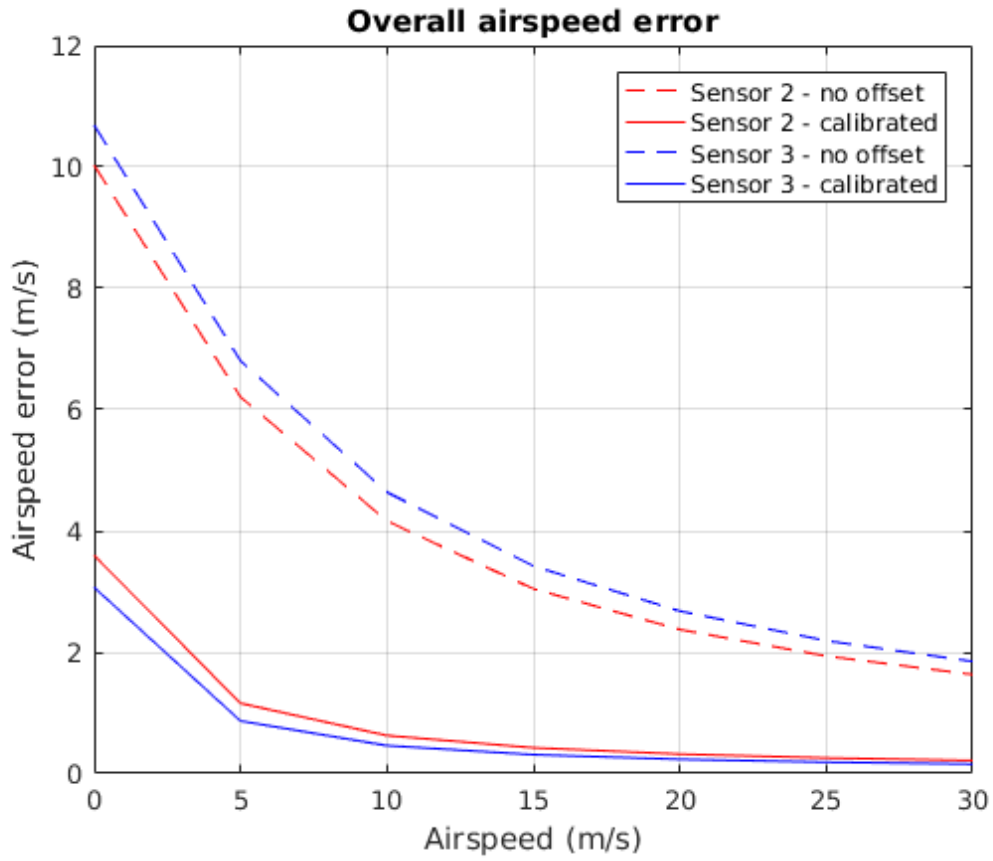

Figure 10.14: Airspeed error due to sensor error

10.3 The effect of the wing on differential pressure measurements

Perhaps the most significant result of this series of experiments is a characterization on the effect of the presence of the wing on the differential pressure measurements. If the impact of the wing is great, then the Pitot-static probe choice should be reviewed and possibly a different design should be selected.

Performance of the existing calibration model

To begin, we examine the performance of the previously calibrated airspeed sensor models on this new installation. The compensated differential pressure measurements compared to the reference differential pressure, for sensors 1, 2 and 3, for all `wc_*` datasets, can be seen in Figures 10.15, 10.16 and 10.17. It is clear that the previous calibration model has a larger error, when the wing is installed, as seen in Table 10.8.

It is noteworthy that the longer probe of sensor 1 is significantly less susceptible

to the effect of the wing, whereas the shorter probe of sensors 2 and 3 is now well within the perturbations that the wing causes. As a result, the model error is larger compared to the error corresponding to a bare (no wing) installation.

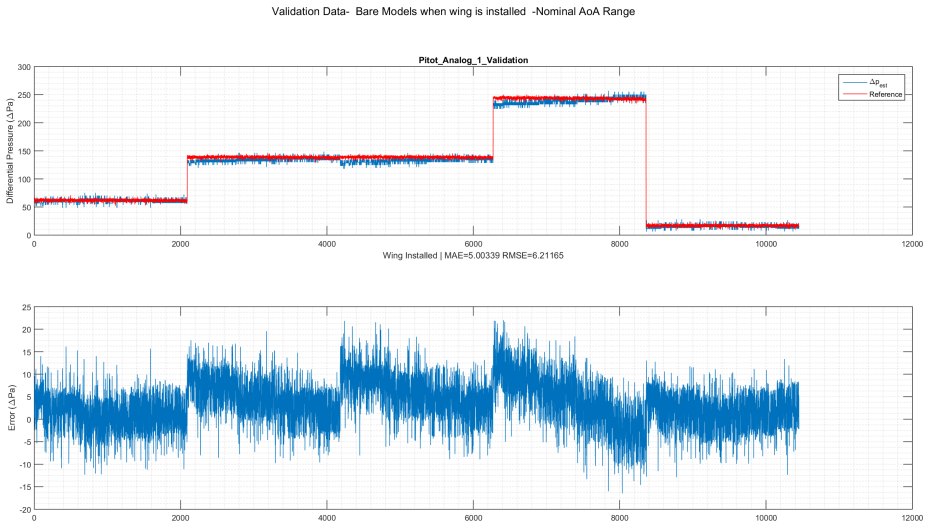

Figure 10.15: Model validation for airspeed sensor 1 - existing calibration - nominal range

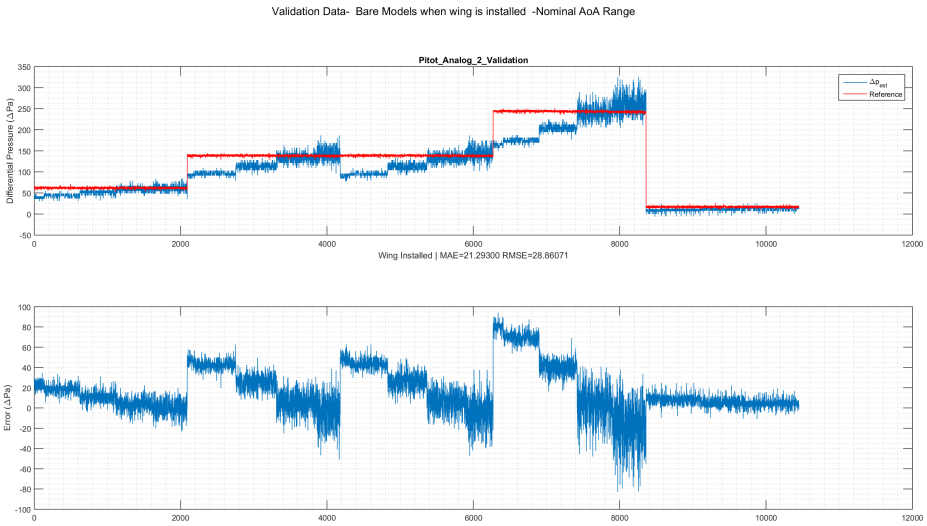

Figure 10.16: Model validation for airspeed sensor 2 - existing calibration, nominal range

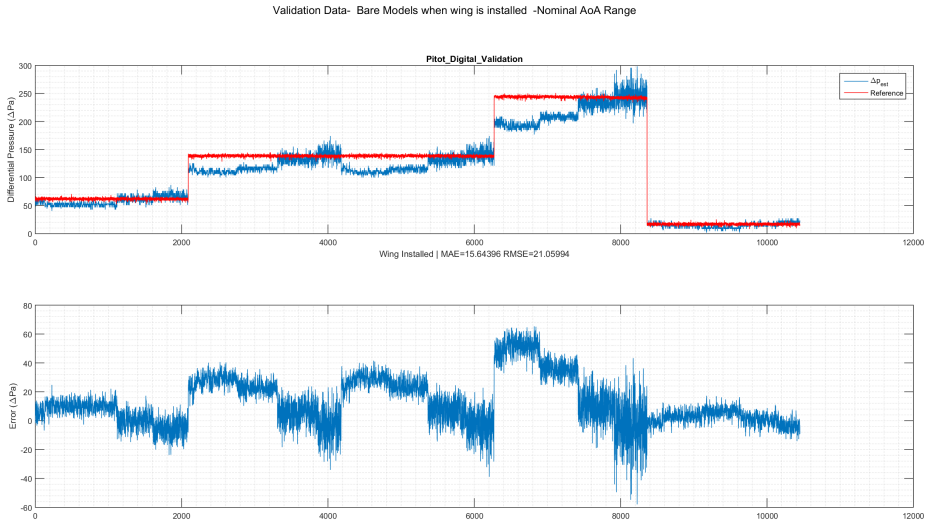

Figure 10.17: Model validation for airspeed sensor 3 - existing calibration, nominal range

Instrument	sensor 1	sensor 2	sensor 3
MAE (Pa)	5.00	21.29	15.64
RMSE (Pa)	6.21	28.86	21.06

Table 10.8: Error metrics for probes 1,2,3 under nominal AoA conditions - no wing calibration profile

To demonstrate the increased impact of AoA when the wing is installed, Figures 10.18 ,10.19 and 10.20 present the measurement error, compensated for the initial, no wing calibration, versus the reference pressure, for the extreme AoA regions of the `wc_20` experiment. Table 10.9 summarizes the error characteristics.

Instrument	probe 1	probe 2	probe 3
MAE (Pa)	5.59	20.00	15.32
RMSE (Pa)	7.30	27.32	20.92

Table 10.9: Error metrics for probes 1,2,3 under extreme AoA conditions, no wing calibration profile

Again, the longer probe of sensor 1 outperforms sensors 2,3 considerably.

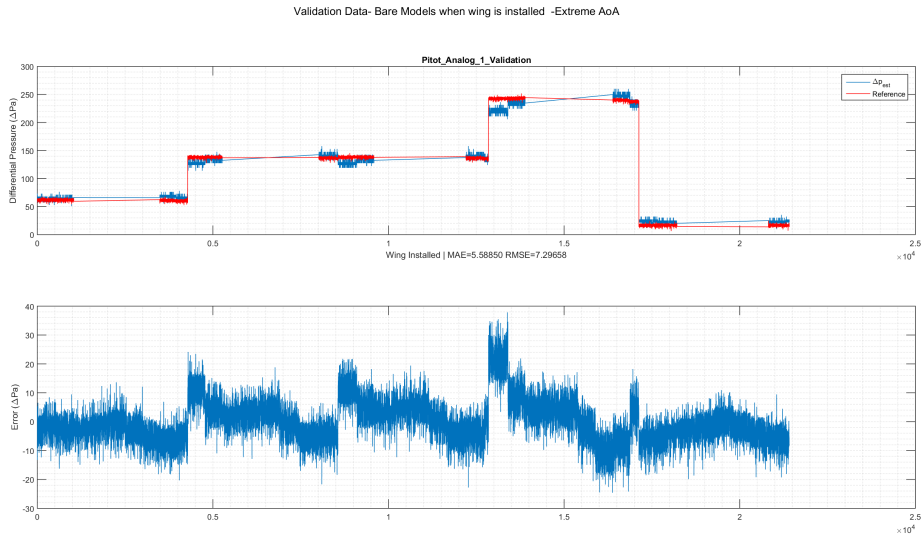

Figure 10.18: Model validation for airspeed sensor 1 - existing calibration, extreme AoA

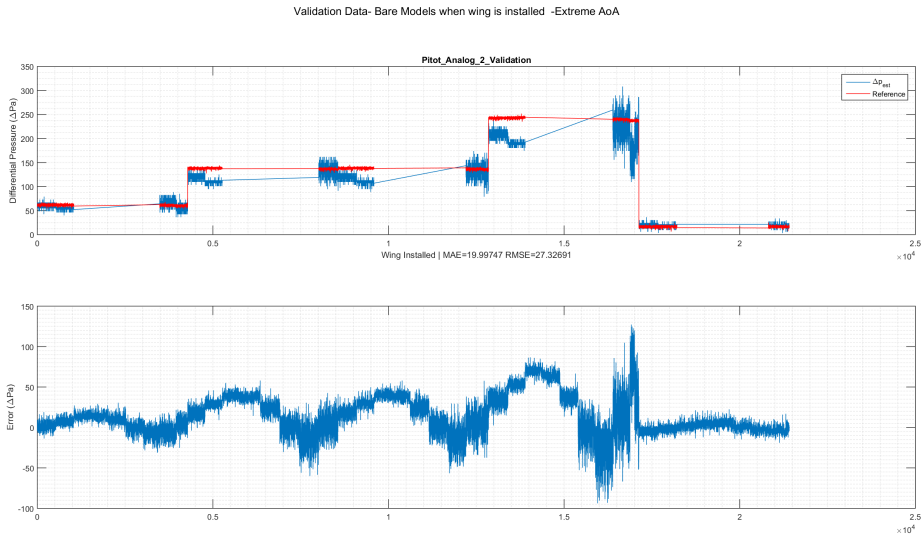

Figure 10.19: Model validation for airspeed sensor 2 - existing calibration, extreme AoA

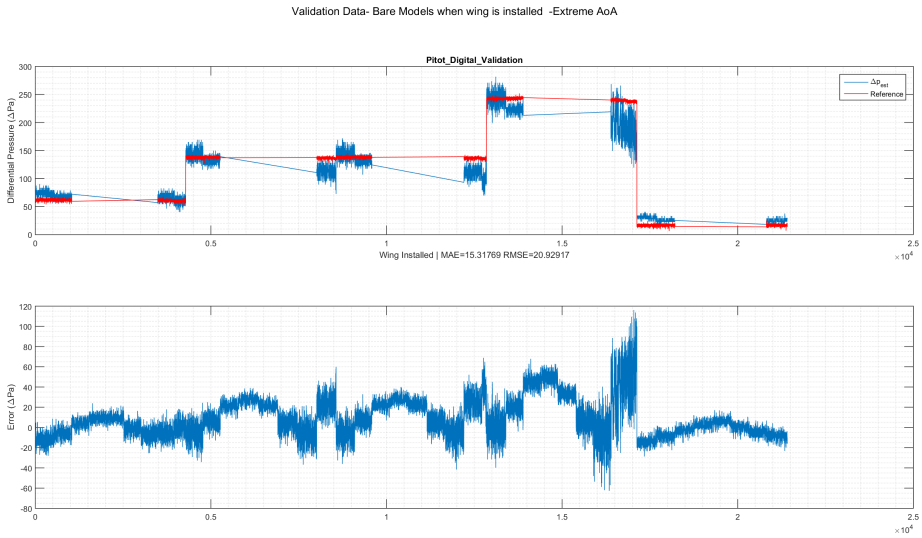

Figure 10.20: Model validation for airspeed sensor 3 - existing calibration, extreme AoA

New calibration model

It is worthwhile to try extracting a new calibration model for all sensors to compensate for the effect of the wing. Once again, calibration efforts focused on two AoA ranges: the nominal ($\alpha \in [-5, 15]^\circ$) and the extended one ($\alpha \in [-20, 25]^\circ$). Thus, two models were extracted and validated in the corresponding ranges for each sensor. Training and validation datasets were presented in the Data Partitioning section.

At this point, a brief comment must be made regarding the trade-off between simple models and accuracy. In low cost UAV implementations, sensor models are usually computed for state estimation purposes. Thus, complex sensor models composed of strongly non-linear terms may obstruct the development of efficient and straightforward sensor fusion algorithms. In the case of Extended Kalman Filtering, such models can degrade observability or may even cause estimates to diverge. Consequently, it is common practice to avoid the use of complicated transfer functions when no significant reduction on the estimation errors can be achieved. In the case of pitot probes and in nominal AoA ranges, we chose to limit the pool of candidate regressors in $\{P_{d,r}\}$.

Regression coefficients can be seen in Tables 10.10, 10.12 for the nominal and extended ranges respectively. For the latter case, we also present the maximum contributions (in Pa) of each model term in Table 10.13.Statistical metrics on errors can be seen on Tables 10.11,10.14

Figures 10.21, 10.22 ,10.23 and 10.27, 10.28 ,10.29 display the model fit results and fitting errors while Figures 10.24, 10.25 , 10.26 and 10.30, 10.31 , 10.32 show the prediction error for the validation run. Extracted models from training data cannot fit very well the measured data of sensors 2,3 as seen by the relative coefficients of determination (R^2) in Table 10.12.

Validation results for the new calibration model **do not** indicate a satisfactory compensation of the error introduced by the wing installation. Possible reasons for model insufficiency may also include the calibrator's geometry combined with a suboptimal airfoil embedding. However,it should be noted that sensor 1 along with the longer probe performed very well under all circumstances. The relevant error metrics are shown on Table 10.14.

instrument	$\theta_{P_{d,r}}$	R^2
sensor 1	0.9532 $\pm$0.0002	0.9932
sensor 2	0.7590 $\pm$0.0007	0.8587
sensor 3	0.7159 $\pm$0.0004	0.9302

Table 10.10: Probe coefficients on reduced α range-Wing Installed

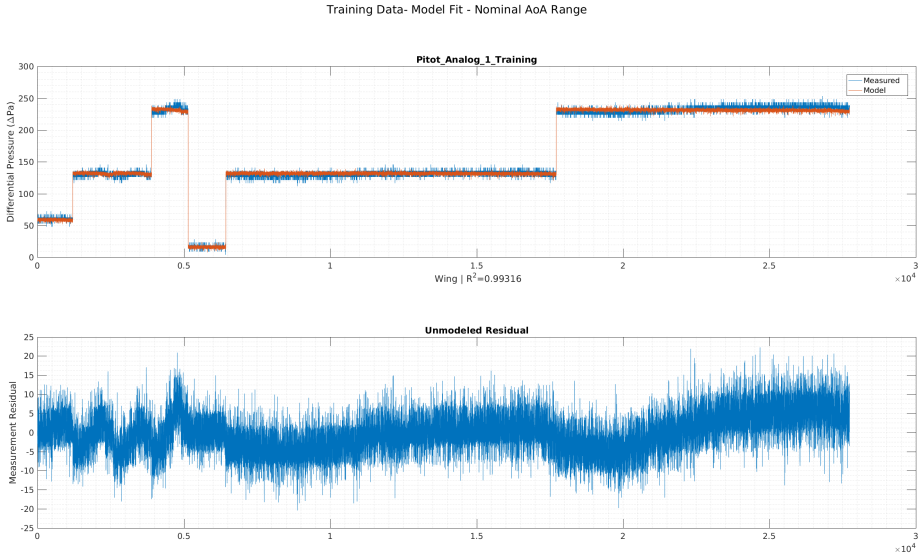

Figure 10.21: Calibration results for sensor 1 with wing installed - Nominal AoA range

instrument	probe 1	probe 2	probe 3
MAE (Pa)	4.38	21.70	14.67
RMSE (Pa)	5.56	27.46	18.75

Table 10.11: Error metrics for probes 1,2,3 on nominal α range with wing

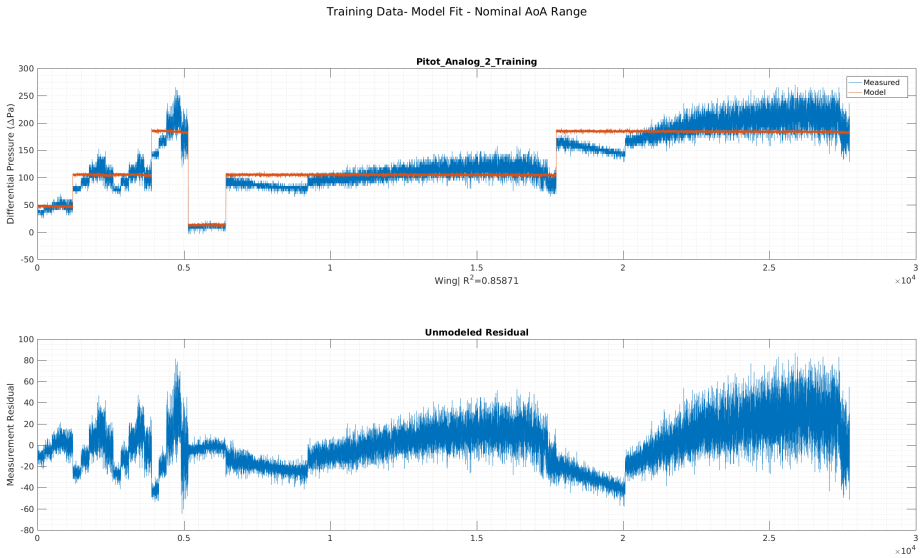

Figure 10.22: Calibration results for sensor 2 with wing installed - Nominal AoA range

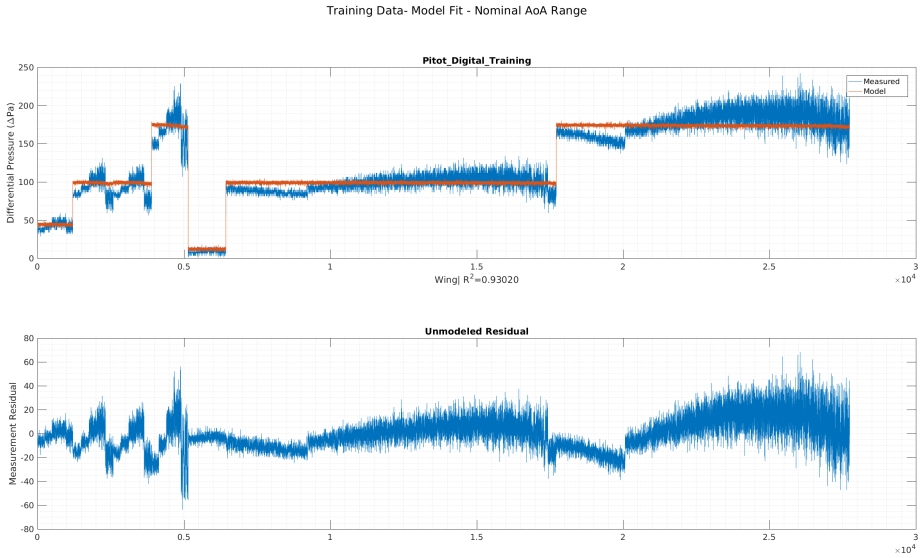

Figure 10.23: Calibration results for sensor 3 with wing installed - Nominal AoA range

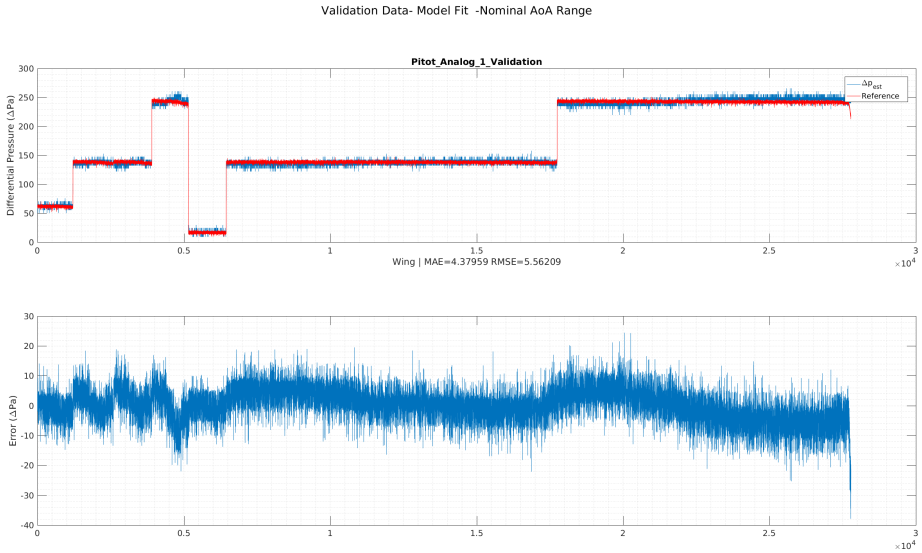

Figure 10.24: Validation results for sensor 1 with wing installed - Nominal AoA range

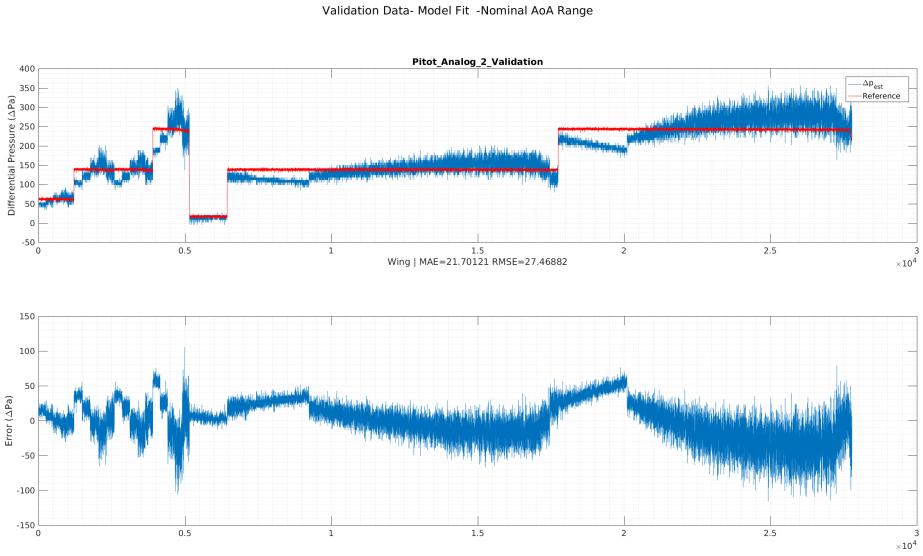

Figure 10.25: Validation results for sensor 2 with wing installed - Nominal AoA range

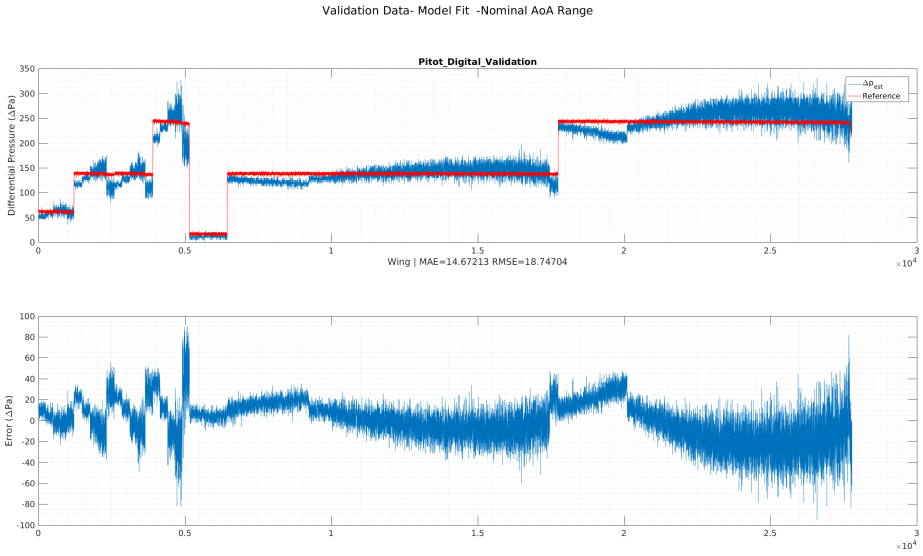

Figure 10.26: Validation results for sensor 3 with wing installed - Nominal AoA range

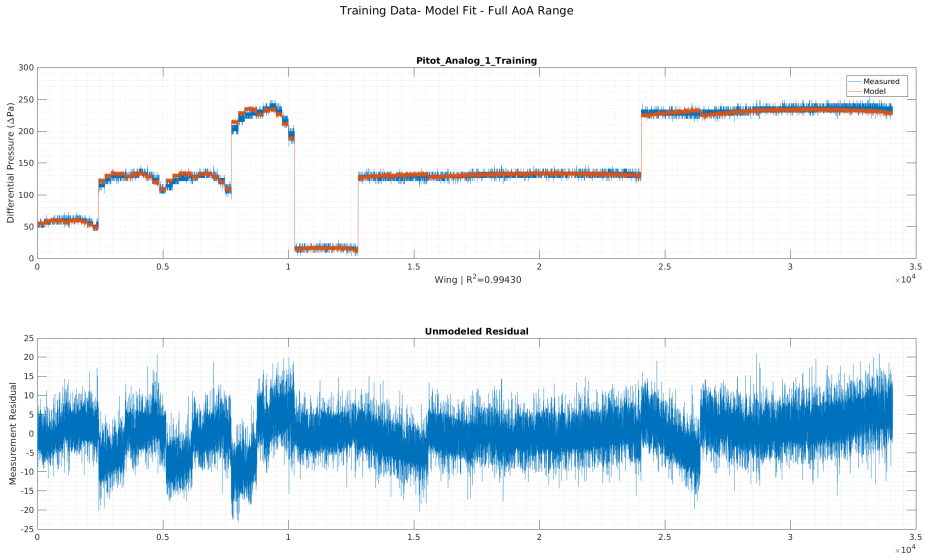

Figure 10.27: Calibration results for sensor 1 with wing installed - Full AoA range

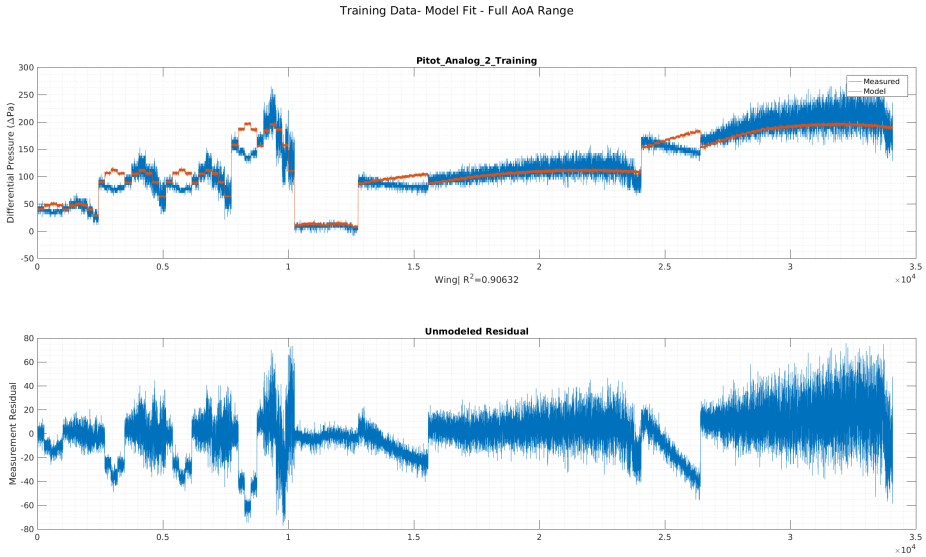

Figure 10.28: Calibration results for sensor 2 with wing installed - Full AoA range

While the differential pressure estimates for all sensors have definitely better noise characteristics, one should keep in mind that the wind tunnel experiment and the ensuing calibration are not trivial procedures. The reduction in calibration effort that a longer probe, immune to wing impact, can offer should not be underestimated.

The non-deterministic nature of the validation error on Figures 10.31 and 10.32 warrants a comment. It may seem that there have been mistakes in the application

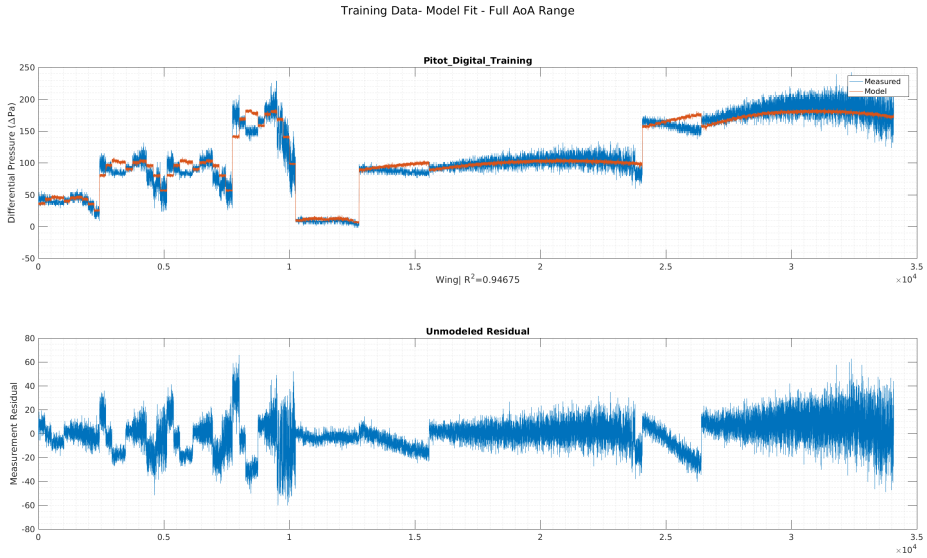

Figure 10.29: Calibration results for sensor 3 with wing installed - Full AoA range

instrument	θ_0	θ_1	θ_2	R^2
sensor 1	0.9212 $\pm 3.39 \cdot 10^{-4}$	0.0103 $\pm 7.81 \cdot 10^{-5}$	-0.0006111 $\pm 3.67 \cdot 10^{-6}$	0.9943
sensor 2	0.6319 $\pm 1.20 \cdot 10^{-3}$	0.0339 $\pm 2.76 \cdot 10^{-4}$	-0.0016 $\pm 1.29 \cdot 10^{-5}$	0.9063
sensor 3	0.6445 $\pm 8.30 \cdot 10^{-4}$	0.0231 $\pm 1.91 \cdot 10^{-4}$	-0.0013 $\pm 8.99 \cdot 10^{-6}$	0.9468

Table 10.12: Probe coefficients on full α range with wing

of the model fit procedure, and using a different regressor pool could produce better results. However, when the Ordinary Least Squares (OLS) method is selected, which is a common approach, the assumption that white, Gaussian noise corrupts the measurements is made. However, as is clearly visible in Figure 10.33, this is not the case for the combination of short probes and wing installed. As a result, the method fails to produce good results, since it is used outside of its scope.

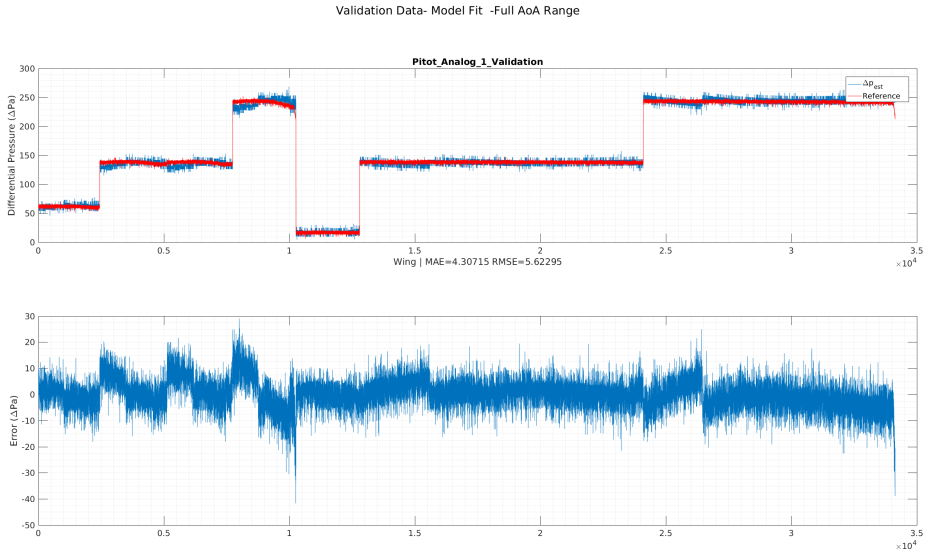

Figure 10.30: Validation results for sensor 1 with wing installed - Full AoA range

instrument	$\theta_0 P_{d,r}$	$\theta_1 \lvert\alpha\rvert P_{d,r}$	$\theta_2 \alpha^2 P_{d,r}$
sensor 1	232.73	60.66	88.07
sensor 2	159.65	198.66	237.07
sensor 3	162.83	135.51	189.05

Table 10.13: Maximum Regressor Contribution in (Pa) on full α range (wing installed)

instrument	probe 1	probe 2	probe 3
MAE (Pa)	4.30	17.84	13.66
RMSE (Pa)	5.62	24.20	19.03

Table 10.14: Error metrics for probes 1,2,3 on full α range with wing

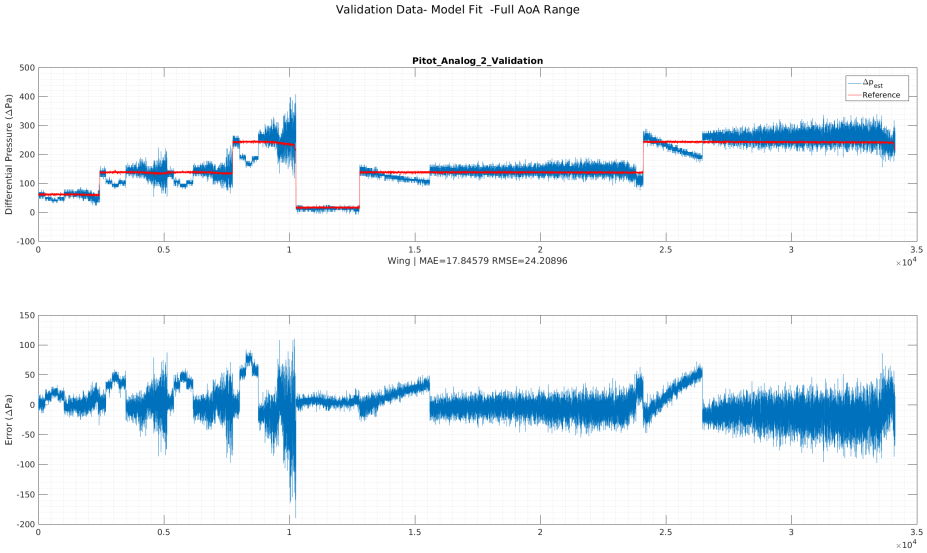

Figure 10.31: Validation results for sensor 2 with wing installed - Full AoA range

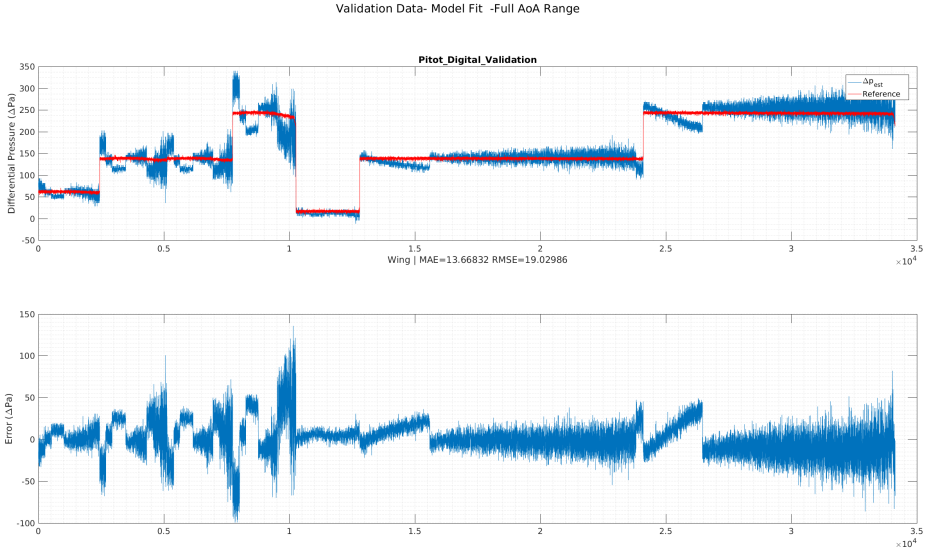

Figure 10.32: Validation results for sensor 3 with wing installed - Full AoA range

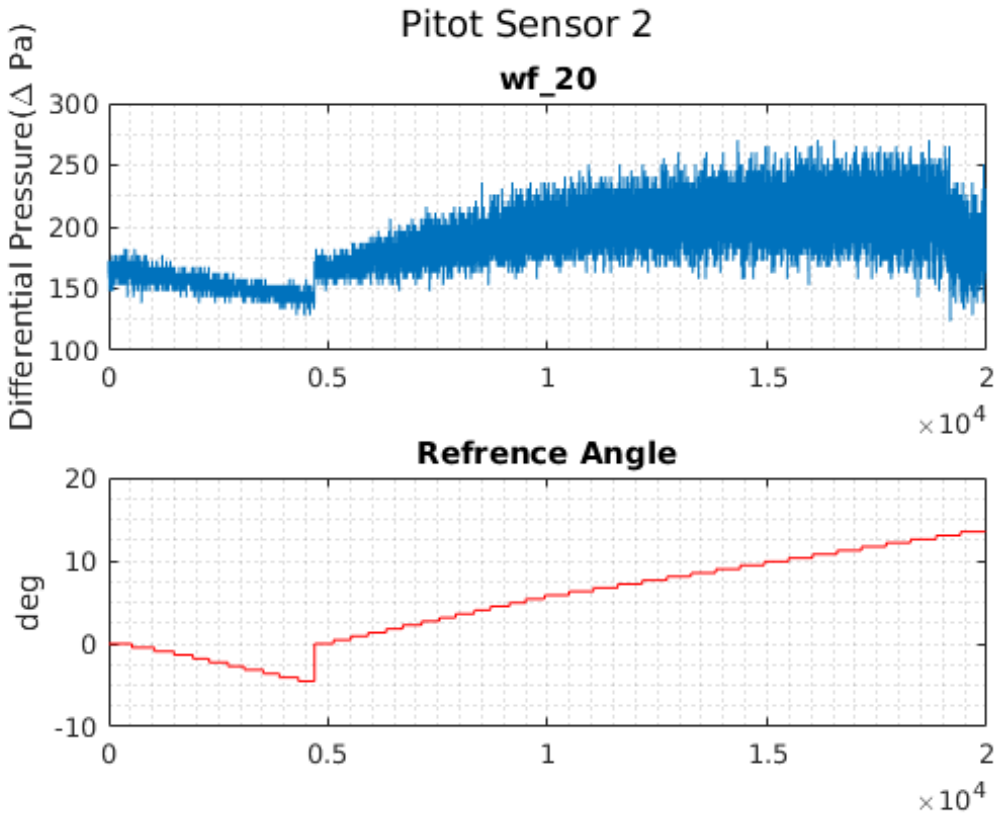

Figure 10.33: Non-Gaussian noise on the airspeed sensor 2 measurements, with wing installed

10.4 Error statistics on airspeed conversion

Since one of the two initial goals of this work was to obtain accurate estimates of the airspeed, using Pitot-static probes, an error analysis should be performed. The equation for the derivation of airspeed, given the differential pressure and air density, was given in 10.2. Differential pressure is directly measured (and possibly compensated) but air density is not. Instead, the formula

$$\rho = \frac{P_s M_0}{R^* T} \tag{10.3}$$

is commonly used. P_s is the static pressure. M_0 is the mean molecular weight of the air, with a default value of $0.028\,964\,4\,\mathrm{kg\,mol^{-1}}$. R^* is the gas constant, for which the US Standard Atmosphere [6] specifies $8.314\,32\,\mathrm{N\,m\,mol^{-1}\,K^{-1}}$ as a default value. T is the temperature of the air, in K.

$R_{specific} = \frac{R^*}{M_0}$, the specific gas constant for dry air, for the above values, is evaluated at $287.053\,\mathrm{J\,kg^{-1}\,K^{-1}}$.

With this nominal value, ρ can be evaluated by

$$\rho = \frac{P_s}{287.053T} \tag{10.4}$$

Static pressure measurement

Ideally, for the reasons presented previously in this chapter, the absolute static pressure measurement should be captured from the static port on a Pitot-static probe sampling clean air. This requires a T-junction on the pressure tubing coming out of the static port, so that both the differential pressure sensor and the barometer can have access to the measurement. However, in our experimental installation this was not the case: A separate barometer was installed on the same location as the differential pressure sensors. This is also the case in most low-cost commercial UAVs, where a separate barometer device is placed inside the UAV fuselage.

This raises the question: how accurate is the measurement of this device, in regard to position errors, stemming from the installation of the sensor, not the sensor deficiencies themselves. In other words, how much worse is the measurement, when the static pressure is sampled without a static pressure probe?

Let us examine the measurement error without and with a wing installed. As reference value the mean barometric pressure as measured from the same device, on $0\,\mathrm{m\,s^{-1}}$, is selected. Data from experiments

- bc_0, bc_5, bc_10, bc_15, bc_20, bc_25, bc_30, bc_35, bc_40

are used for the no-wing run, and data from

- wc_0, wc_20

are used for the "with-wing" run. Figure 10.34 shows barometer measurements without a wing installed, while Figure 10.35 shows the two available barometer data sets with a wing installed. The mean values of the data sets are reported in Table 10.15.

The two different test runs were performed on different days, so a difference on the readings at $0\,\mathrm{m\,s^{-1}}$ is understandable.

There is a clear trend where recorded pressure decreases with increasing airspeed. Depending on where the barometer is installed, either on low pressure or high pressure areas, of the surrounding geometry, the readings are expected to shift. The same effect is observed when the barometer is covered and protected by the wing, but to a lesser extent.

In the range $0\,\mathrm{m\,s^{-1}}$ to $20\,\mathrm{m\,s^{-1}}$, a difference of 45 and 148 Pa in static pressure was observed with and without a wing installed, respectively.

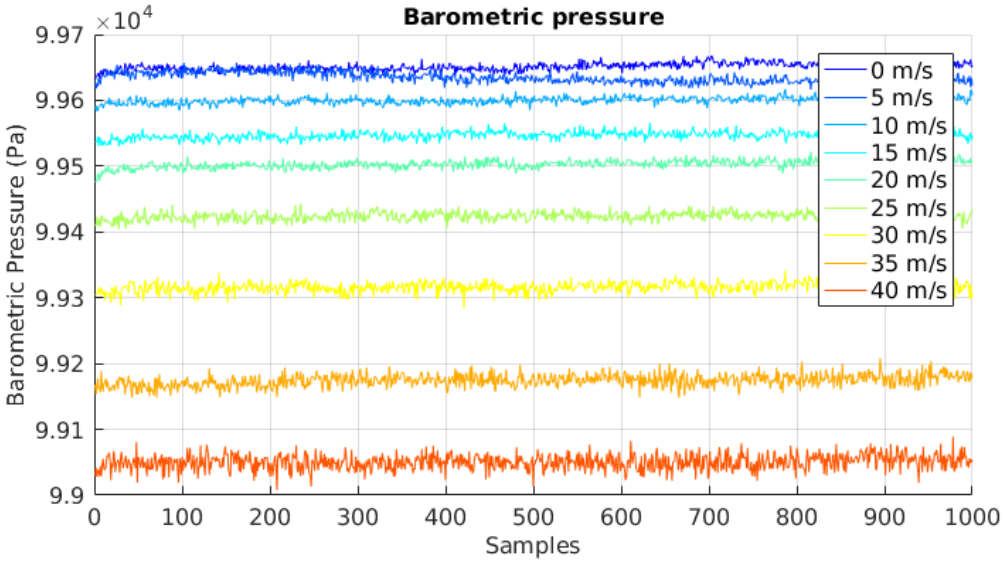

Figure 10.34: Barometer samples for various airspeeds - no wing

Temperature measurement

For similar reasons as above, the air temperature should be read on free-stream air, not inside the fuselage. Electronics are commonly placed close to each other inside the fuselage and generate heat, corrupting thermometer readings. Fortunately, the DS4525DO sensor has an embedded thermometer which should theoretically measure the air temperature as measured by the Pitot-static probe, even though this might have some errors as well [1]. In Figures 10.36 and 10.37 temperature time series from both the barometer and the differential pressure sensor are shown,

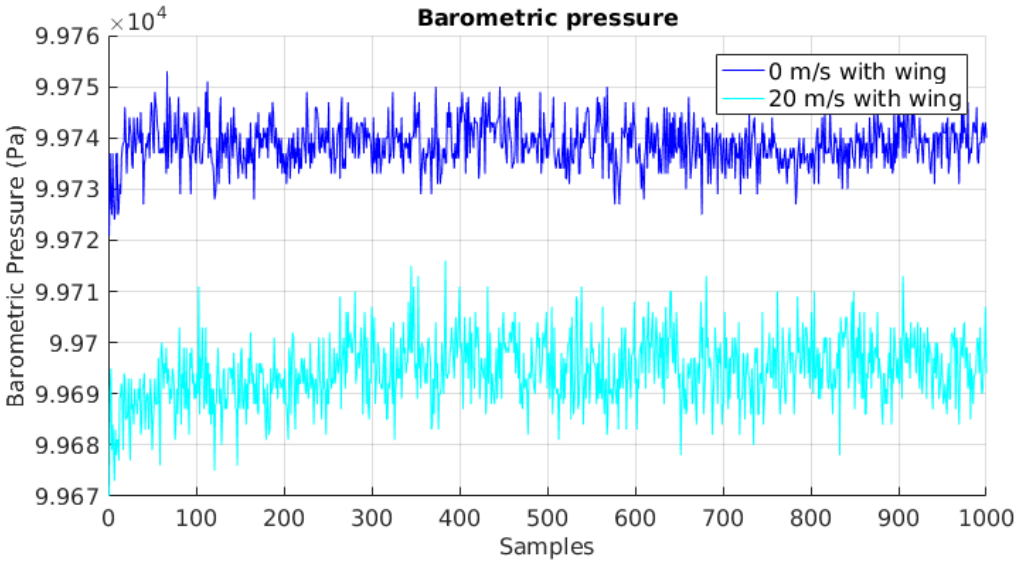

Figure 10.35: Barometer samples for various airspeeds - with wing

Airspeed (m/s)	Wing Installed?	Mean Pressure (Pa)
0	N	99651
5	N	99635
10	N	99600
15	N	99547
20	N	99503
25	N	99424
30	N	99316
35	N	99174
40	N	99050
0	Y	99739
20	Y	99694

Table 10.15: Mean values of barometer data series

based on the `bc_*` runs. The barometer temperature readings were printed as integer values.

Temperature recorded from the barometer seems to drop, when there is a great increase in airspeed. This can be attributed to the cooling effect of the fast airflow over the sensor.

The recordings of the differential pressure sensor are less straightforward. At $0\,\mathrm{m\,s^{-1}}$ the measured value is at 19.5 °C, gradually drops to 17.2 °C as airspeed approaches $15\,\mathrm{m\,s^{-1}}$ and the raises again at 19.5 °C, with some AoA dependency.

One could argue that initially the differential pressure sensor could have some temperature bias due to self-generated heat, which then subsided with increased airflow.

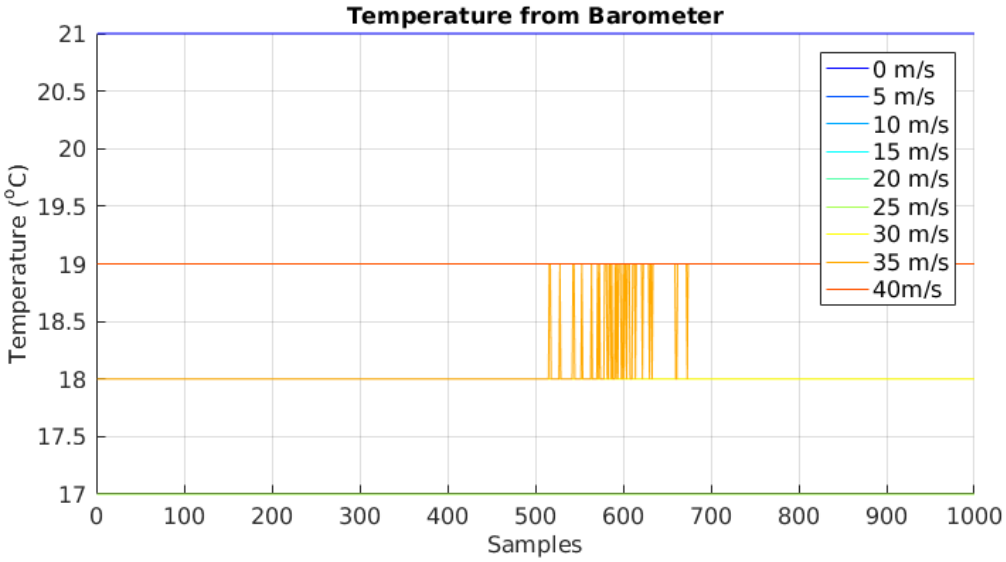

Figure 10.36: Temperature samples from barometer for various airspeeds - no wing

However, it is also very likely that the wind tunnel air mass temperature increased in high airspeeds, due to friction and induction heating from the fan motor, explaining the increase in temperature.

The same response, more or less, was recorded with a wing installed on top of the sensors. The wing did not protect the sensors significantly from the incoming airflow, so temperature variations correlated to airspeed were once again observed.

Without a wing installed, in the range $0\,\mathrm{m\,s^{-1}}$ to $20\,\mathrm{m\,s^{-1}}$, a difference of 4 and 1.64 °C in temperature was observed in the barometer and differential pressure sensors thermometers respectively.

With a wing installed, in the range $0\,\mathrm{m\,s^{-1}}$ to $20\,\mathrm{m\,s^{-1}}$, a difference of 2 and 1.09 °C in temperature was observed in the barometer and differential pressure sensors thermometers respectively.

Error propagation - Effect of absolute pressure error on air density

On the previous subsection, an approximate range of the absolute pressure and temperature errors over the entire airspeed range was found. In both cases, the accuracy specifications of each sensor were lower than the observed errors, which implies that error sources stemming for the measurement procedure and installation affect the measurements.

Let us investigate the effect of the above errors on air density calculation, as an intermediate step towards airspeed calculation error. The equation 10.4 will be used.

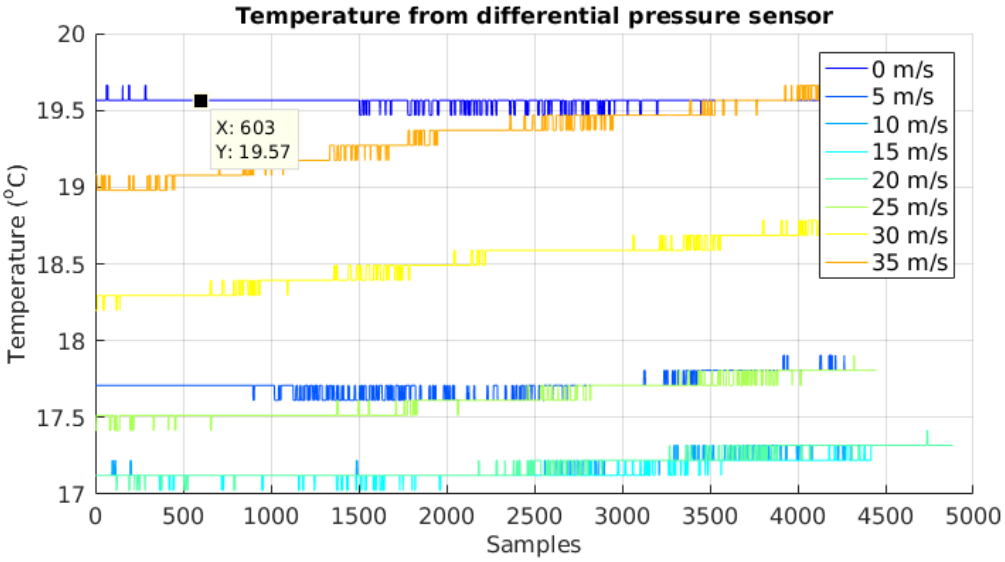

Figure 10.37: Temperature samples from differential pressure sensor for various airspeeds - no wing

For a nominal temperature of 25 °C and static pressure 101 325 Pa, the air density error because of absolute pressure measurement error is visualized on Figure 10.38, for various error values.

The relation is linear and is described by the equation

$$\epsilon_\rho = \frac{\epsilon_{P_s}}{287.053T} \tag{10.5}$$

Error propagation - Effect of temperature error on air density

Similarly to the previous error investigation, we shall plot the error on air density calculation for a range of temperature errors, for a nominal temperature of 25 °C and static pressure of 101 325 Pa. The results can be seen in Figure 10.39. This time the relation is not linear but it can be approximated linearly with very good accuracy in the range of interest, by the equation:

$$\epsilon_\rho = \left.\frac{\partial \rho}{\partial \epsilon_T}\right|_{P,T} \epsilon_T = 3.965 \times 10^{-3} \epsilon_T \tag{10.6}$$

Error propagation - Effect of air density error on airspeed

In the previous subsection, it was observed that, given the expected errors on temperature and static pressure measurements, the error on air density calculation is mostly governed by the temperature errors, by an order of magnitude.

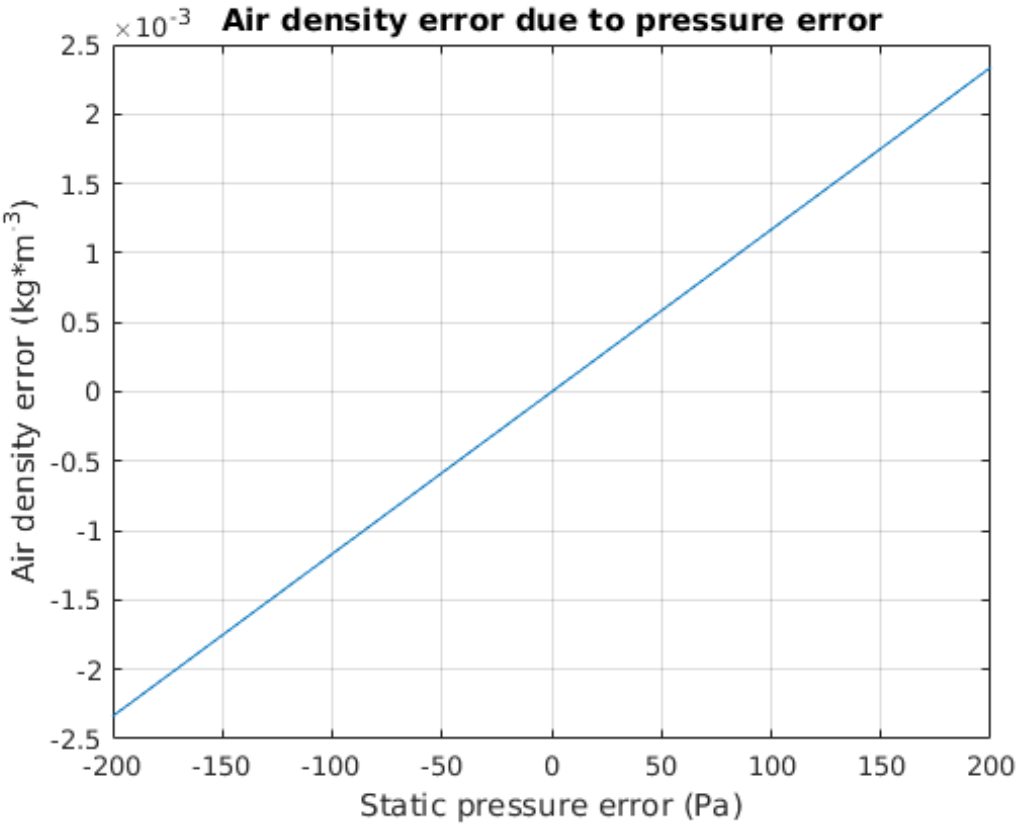

Figure 10.38: Air density error due to static pressure measurement error

With these coarse figures, regarding the error bounds of air density, due to both absolute pressure and temperature measurements, we can proceed by calculating the effect of air density errors on airspeed calculations.

For a range of airspeeds of $V_a \in [0, 20]\,\mathrm{m\,s^{-1}}$ and a range of air density error $-0.03\,\mathrm{kg\,m^{-3}}$ to $0.03\,\mathrm{kg\,m^{-3}}$, for a nominal air density of $1.1839\,\mathrm{kg\,m^{-3}}$, the error on airspeed calculation because of air density error can be seen in Figure 10.40.

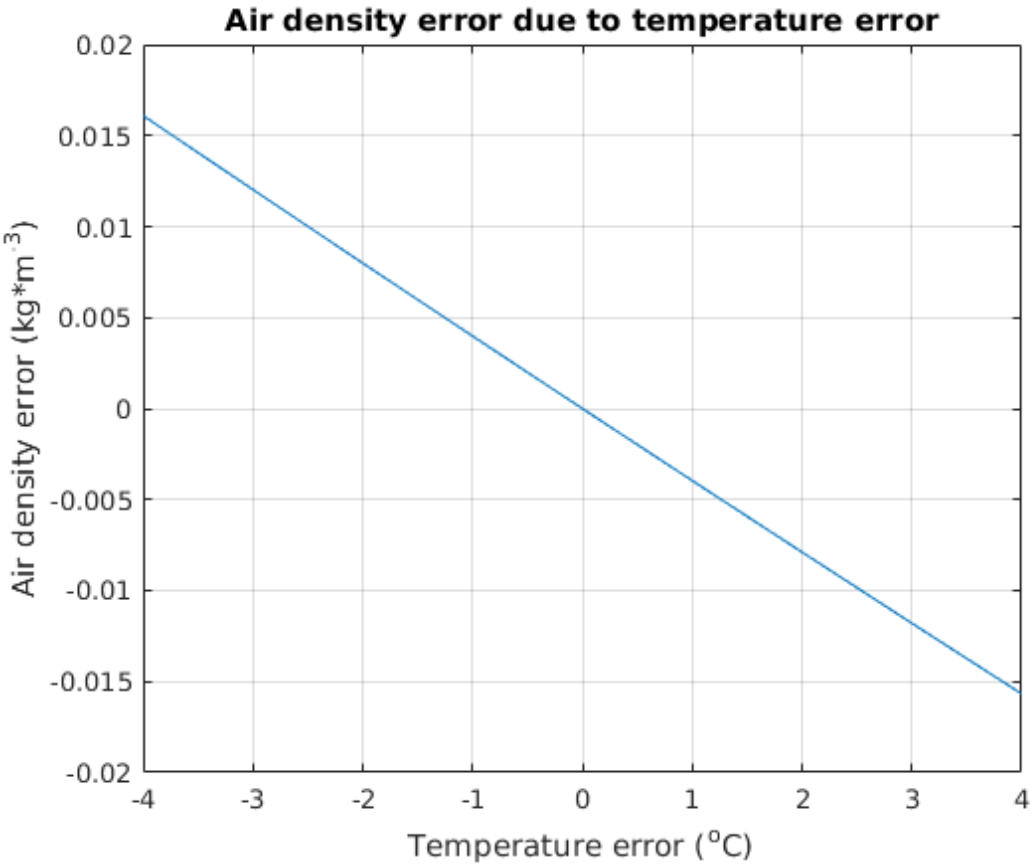

Figure 10.39: Air density error due to temperature measurement error

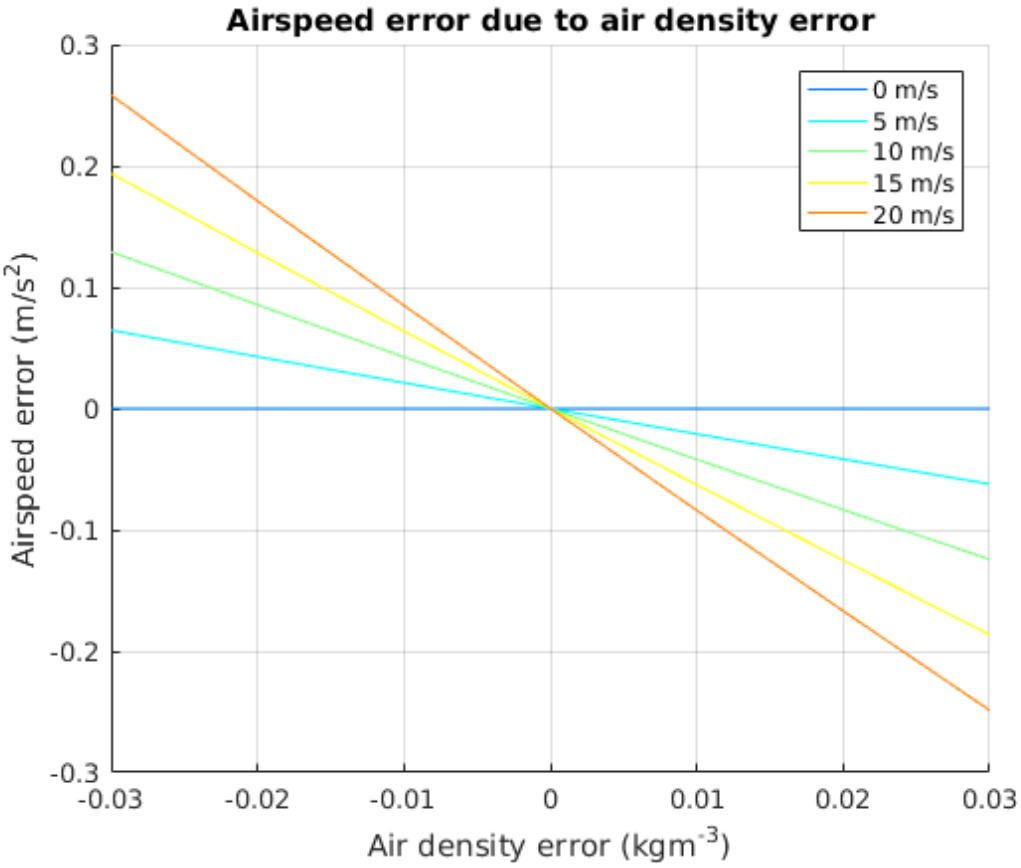

Figure 10.40: Airspeed error due to air density

Appendix A

Summarized Calibration Coefficients

A.1 AoA Vanes

AoA sensor 1 calibration coefficients - full AoA range		
Parameter name	**Parameter value**	**Error bounds (95% - white)**
θ_0	3.9017	$\pm$0.0054
θ_α	1.1370	$\pm$0.0007
R^2	0.9923	

AoA sensor 2 calibration coefficients - full AoA range		
Parameter name	**Parameter value**	**Error bounds (95% - white)**
θ_0	4.2905	$\pm$0.0056
θ_α	0.9518	$\pm$0.0018
R^2	0.9898	

AoA sensor 3 calibration coefficients - full AoA range		
Parameter name	**Parameter value**	**Error bounds (95% - white)**
θ_0	0.6730	$\pm$0.0052
θ_α	0.9760	$\pm$0.006
R^2	0.9902	

AoA sensors model validation - full AoA range			
Error metric	Sensor 1	Sensor 2	Sensor 3
MAE (deg)	0.54437	0.65930	0.7477
RMSE (deg)	0.68751	0.90803	0.89947

AoA sensors model validation - nominal AoA range			
Error metric	Sensor 1	Sensor 2	Sensor 3
MAE (deg)	0.42679	0.70464	0.63591
RMSE (deg)	0.54380	0.94537	0.75422

A.2 Airspeed sensors

Extracted Models when no wing is installed

Pitot Probes Calibration Coefficients-Full AoA Range				
instrument	θ_0	θ_1	θ_2	R^2
sensor 1	0.9523 $\pm 2.97 \cdot 10^{-4}$	0.049 $\pm 5.76 \cdot 10^{-5}$	-0.00031 $\pm 3.91 \cdot 10^{-6}$	0.9988
sensor 2	0.7963 $\pm 5.02 \cdot 10^{-4}$	0.003 $\pm 9.70 \cdot 10^{-5}$	-0.00021 $\pm 3.91 \cdot 10^{-6}$	0.9955
sensor 3	0.7809 $\pm 4.86 \cdot 10^{-4}$	0.038 $\pm 9.39 \cdot 10^{-5}$	-0.00030 $\pm 3.78 \cdot 10^{-6}$	0.9955

Maximum Regressor Contribution in Pa -Full AoA Range			
instrument	$\theta_0 P_{d,r}$	$\theta_1 \lvert\alpha\rvert P_{d,r}$	$\theta_2 \alpha^2 P_{d,r}$
sensor 1	719.21	90.56	139.77
sensor 2	601.42	54.61	92.50
sensor 3	589.76	68.90	135.18

Pitot Probes Modelling Errors-Full AoA Range			
instrument	sensor 1	sensor 2	sensor 3
MAE (Pa)	4.7006	8.4332	8.6530
RMSE (Pa)	6.7832	13.7502	14.1424

Pitot Probes Calibration Coefficients-Nominal AoA Range		
instrument	$\theta_{P_{d,r}}$	R^2
sensor 1	0.9670 ± 0.0001	0.9991
sensor 2	0.8100 ± 0.0002	0.9967
sensor 3	0.7826 ± 0.0002	0.9973

Pitot Probes Modelling Errors-Nominal AoA Range			
instrument	sensor 1	sensor 2	sensor 3
MAE (Pa)	3.8047	6.7009	6.4057
RMSE (Pa)	4.9923	9.8628	8.9747

Extracted Models after the wing installation

Pitot Probes Calibration Coefficients-Full AoA Range				
instrument	θ_0	θ_1	θ_2	R^2
sensor 1	0.9212 $\pm 3.39 \cdot 10^{-4}$	0.0103 $\pm 7.81 \cdot 10^{-5}$	-0.0006111 $\pm 3.67 \cdot 10^{-6}$	0.9943
sensor 2	0.6319 $\pm 1.20 \cdot 10^{-3}$	0.0339 $\pm 2.76 \cdot 10^{-4}$	-0.0016 $\pm 1.29 \cdot 10^{-5}$	0.9063
sensor 3	0.6445 $\pm 8.30 \cdot 10^{-4}$	0.0231 $\pm 1.91 \cdot 10^{-4}$	-0.0013 $\pm 8.99 \cdot 10^{-6}$	0.9468

Maximum Regressor Contribution in Pa **-Full AoA Range**			
instrument	$\theta_0 P_{d,r}$	$\theta_1 \lvert\alpha\rvert P_{d,r}$	$\theta_2 \alpha^2 P_{d,r}$
sensor 1	232.73	60.66	88.07
sensor 2	159.65	198.66	237.07
sensor 3	162.83	135.51	189.05

Pitot Probes Modelling Errors-Full AoA Range			
instrument	probe 1	probe 2	probe 3
MAE (Pa)	4.30	17.84	13.66
RMSE (Pa)	5.62	24.20	19.03

Pitot Probes Calibration Coefficients-Nominal AoA Range		
instrument	$\theta_{P_{d,r}}$	R^2
sensor 1	0.9532 ± 0.0002	0.9932
sensor 2	0.7590 ± 0.0007	0.8587
sensor 3	0.7159 ± 0.0004	0.9302

Pitot Probes Modelling Errors-Nominal AoA Range			
instrument	probe 1	probe 2	probe 3
MAE (Pa)	4.38	21.70	14.67
RMSE (Pa)	5.56	27.46	18.75

Bibliography

[1] Air density and temperature |. URL: http://www.basicairdata.eu/knowledge-center/background-topics/density-and-air-temperature/.

[2] DELFTACOPTER - DELFTACOPTER. URL: http://www.delftacopter.nl/delftacopter/.

[3] Eagle Tree Systems. URL: http://www.eagletreesystems.com/.

[4] JUMP 20 | Arcturus UAV. URL: http://arcturus-uav.com/product/jump-20.

[5] PaparazziUAV. URL: http://wiki.paparazziuav.org/wiki/Main{_}Page.

[6] US Standard Atmosphere, 1976. Technical report, National Oceanic and Atmospheric Administration, National Aeronautics and Space Adminisration, United States Air Force, 1976. URL: http://scholar.google.com/scholar?hl=en{&}btnG=Search{&}q=intitle:US+Standard+Atmosphere+1976{#}0.

[7] Indicated airspeed, nov 2016. URL: https://en.wikipedia.org/w/index.php?title=Indicated{_}airspeed{&}oldid=751357039.

[8] James Ellingson, Thomas Shepard, and Yu-Chen Li. A combined experimental and numerical analysis of UAV Pitot-static system error at low Reynolds number. In *2014 IEEE Metrology for Aerospace (MetroAeroSpace)*, pages 122–126. IEEE, may 2014. URL: http://ieeexplore.ieee.org/document/6865906/, doi:10.1109/MetroAeroSpace.2014.6865906.

[9] William Gracey and Elwood F. Scheithauer. Flight investigation of the variation of static-pressure error of a static-pressure tube with distance ahead of a wing and a fuselage. Technical report, NACA, 1951.

[10] Jose Larragueta and George Zogopoulos-Papaliakos. 8mm Pitot-static tube, ESP series. Technical report, BasicAirData, 2014.

[11] W Letko. Investigation of the fuselage interference on a pitot-static tube extending forward from the nose of the fuselage. Technical report, NACA, 1947. URL: http://oai.dtic.mil/oai/oai?verb=getRecord{&}metadataPrefix=html{&}identifier=ADA380812.

[12] David F. Rogers, Borja Martos, and Francisco Rodrigues. Low Cost Accurate Angle of Attack System. Technical report, Embry-Riddle Aeronautical University, 2015.